

1 Validation of Rainfall Data Observed by Using Disdrometer under 2 Wet-Bulb Temperature Conditions

3 Hyeon-Joon Kim¹, Sung-Ho Suh², Jongyun Byun³, Changhyun Jun⁴

4 ¹Center of Oceanic and Meteorological Information, Pukyong National University, Busan, South Korea

5 ²Flight Safety Technology Division, NARO Space Center, Korea Aerospace Research Institute, Goheung, South Korea

6 ³Department of Civil, Environmental and Architectural Engineering, Korea University, Seoul, South Korea

7 ⁴School of Civil, Environmental and Architectural Engineering, Korea University, Seoul, South Korea

8

9 *Correspondence to:* Changhyun Jun (cjun@korea.ac.kr)

10 **Abstract.** This study focuses on the reliability assessment of precipitation data calculated from drop size distribution (DSD)
11 based on disdrometer data observations according to wet-bulb temperature (T_w). Three distinct quality control (QC) methods
12 based on fall velocity were implemented and validated against measurements from tipping-buckets and weighing rain gauges
13 collected from January 2020 to February 2024. The analysis indicated that all QC methods exhibited high reliability
14 (correlation coefficient (CC) > 0.98) for rainfall conditions when T_w was above 5 °C, with a mean absolute percentage error
15 (MAPE) of approximately 8.5%. However, the precision of precipitation measurements exhibited a notable decline when T_w
16 was below 2 °C, as indicated by a CC of less than 0.6 and MAPE exceeding 30%. This reduction in accuracy can primarily
17 be attributed to the outcomes of the QC methods, which rely on the falling velocity, given that raindrops and solid particles
18 were observed within the specified T_w range. When considering the melting of snow particles at T_w ranging from 0 °C to 2 °C,
19 the CC approached 0.9, suggesting enhanced measurement reliability. The findings of this study indicate that T_w is a more
20 effective variable than air temperature (T_{air}) for differentiating the precipitation types. This conclusion arises from the
21 observation that the fall velocity of hydrometeors does not reach the terminal velocity of raindrops, even within the T_{air} range
22 of 1–5 °C, coupled with the broad distribution of fall velocities. The DSD shape demonstrated stability across multiple QC
23 methods when T_w was equal to or greater than 2 °C. In contrast, considerable variations were observed at lower temperatures,
24 where particles with diameters ranging from 1 to 2 mm exhibited irregular distribution patterns at temperatures below 1 °C.
25 These results suggest that DSD parameters should be derived from disdrometer data obtained under conditions where T_w is
26 above 2 °C to ensure the reliability of the findings. This study provides critical insights for improving precipitation
27 measurement techniques and DSD analyses in regions with variable temperature conditions.

28 **1 Introduction**

29 Several factors influence the variability in precipitation development, including atmospheric water vapor content, vertical
30 airflow intensity, and temperature and humidity distributions in the vertical profile (Lintner et al., 2017; Padullés et al.,
31 2022). These factors can be categorized as climatological, geographical, or topographical. Climatological factors include
32 alterations in atmospheric water vapor resulting from long-term temperature changes, developmental shifts associated with
33 temperature variations in the upper and lower atmospheric layers, and thermodynamic effects linked to changes in land cover
34 based on climatic characteristics (Dahlström, 2021; Lu et al., 2024). Geographical and topographical factors include the
35 convergence of water vapor due to mountainous terrain, which facilitates vertical precipitation development (Insel et al.,
36 2010; Lee et al., 2014; Kim et al., 2019), and the generation of vertical flow resulting from increased friction at low levels
37 due to coastal topography (Du and Chen, 2019; Yao et al., 2021). Additionally, precipitation development can be influenced
38 by the temperature differential between the sea and air, particularly when cold air from inland regions moves over water
39 bodies during winter (Steenhurgh, 2020). Various environmental factors can influence the disparities in warm precipitation
40 processes, such as collision-coalescence, evaporation, and accretion, which are contingent upon the vertical development of
41 precipitation types, including stratiform, convective, and typhoon-related precipitation. Similarly, cold precipitation
42 processes such as snow riming, melting, and ice crystal growth are affected by these environmental variables. These factors
43 contribute to the development of diverse hydrometeors including rain, snow, and graupel, which are influenced by
44 temperature variations (Maheskumar et al., 2018; Yi et al., 2021). The differences in the precipitation development processes
45 ultimately lead to variations in the total precipitation observed at the surface. Therefore, it is crucial to acquire data that
46 accurately reflects the microphysical characteristics of precipitation to enhance precipitation monitoring. Furthermore,
47 analyses based on long-term observational data are essential to identify the universal characteristics that account for the
48 temporal variability of precipitation.

49 The utilization of long-term observational data considerably reduces errors, mainly by rectifying inaccuracies in the
50 observational data and eliminating outliers. Even among instruments that measure the same meteorological parameters, the
51 threshold values for outlier removal may vary based on the installation conditions and surrounding environment.
52 Additionally, biases in the observed values can arise owing to variations in the observation area and resolution, which are
53 contingent on the type of instrument employed (Sypka, 2019; Segovia-Cardozo et al., 2021). Ground-based rain gauges can
54 be categorized into two types based on their measurement method: tipping-buckets and weighing gauges. Although the
55 tipping-bucket type demonstrates high accuracy in measuring rainfall, its efficacy in measuring snowfall during winter may
56 be inferior to that of the weighing type because the observation value is recorded only when the precipitation in the bucket
57 reaches a predetermined capacity (Savina et al., 2012; Kochendorfer et al., 2020). Comprehending the characteristics of
58 observational instruments and the data they produce is imperative to ensure the reliability of the research findings derived
59 from observational data.

60 The standard instruments used to observe precipitation include rain gauges and disdrometers. A rain gauge measures the total
61 precipitation accumulated over a specified time interval. In contrast, a disdrometer assesses the size and concentration of
62 precipitation particles, thereby enabling the determination of the precipitation intensity and type. The selection of an
63 appropriate type of rain gauge is contingent on specific observational objectives such as monitoring heavy rain, light rain, or
64 snow. Notable examples of disdrometers include the Particle Size and Velocity (PARSIVEL), Two-dimensional Video
65 Disdrometer (2DVD), Joss-Waldvogel Disdrometer, and Precipitation Occurrence Sensor System. Disdrometers compute the
66 size-specific concentration of particles, known as the Drop Size Distribution (DSD), by analyzing the variations in optical
67 intensity as the particles traverse the observation zone of the sensor. In contrast to data obtained from rain gauges,
68 disdrometer data offer a broader range of applications because they provide physical parameters, such as particle number
69 concentration and fall velocity, and morphological characteristics, such as oblateness.

70 A typical application of disdrometer data involves formulating Quantitative Precipitation Estimation (QPE) equations, which
71 are used in conjunction with remote sensing data such as radar observations. To derive rainfall information from remote
72 sensing data, researchers can leverage the correlation between rain rate and radar reflectivity values, an observational
73 variable in remote sensing, to measure variations in rainfall (Ji et al., 2019; Tang et al., 2024). Additionally, DSD
74 information obtained from disdrometer observations is instrumental in parameterizing microphysical schemes within
75 numerical weather prediction models (Yang et al., 2019; Iversen et al., 2021). Microphysical schemes can be categorized
76 into bin and bulk types (Hu and Igel, 2023). The bin scheme accurately simulates the distributional differences between
77 hydrometeor types by accounting for their size-dependent number concentration. However, this approach is limited by its
78 high computational demand and the need for substantial hardware resources during the simulation process. Consequently,
79 bulk schemes are predominantly employed in weather prediction models. This approach simulates microphysical processes
80 based on the relationships between particle diameter and concentration distributions for various hydrometeor types. The
81 DSD model considerably influences the quantitative differences in the estimated precipitation property outcomes. As the
82 reliability of the DSD model improves, so does the accuracy of the precipitation simulation and forecasting.

83 The DSD model used in the QPE and microphysical schemes of remote sensing encompasses various models, such as the
84 Marshall-Palmer, exponential (Marshall and Palmer, 1948), and gamma models (Ulbrich, 1983). The configuration of each
85 model is contingent on the specific parameters being analyzed, with the shape and slope variables in the DSD model varying
86 according to the concentration distribution based on the particle diameter (Smith, 2003; Liu et al., 2021). The DSD is
87 affected by several factors, such as the type of rainfall (Deo and Walsh, 2016), intensity of rainfall (Thomas et al., 2021), and
88 climatological and topographical characteristics of the region where precipitation occurs and develops (Kim et al., 2022).
89 Consequently, it is imperative to acquire DSD model parameters and reflectivity data by collecting highly reliable
90 observational data that accurately represent precipitation characteristics to enhance the precision of rainfall estimations and
91 simulations based on DSD. Furthermore, disdrometer data can be used to estimate rainfall erosivity (Serio et al., 2019).
92 Enhancing the accuracy of rainfall erosivity estimates can facilitate the assessment of the impact of rainfall on soil erosion
93 and serve as a foundation for developing countermeasures through spatial analysis and monitoring of soil erosion risk areas

94 using remote sensing data. Reliable precipitation observational data for estimating rainfall erosivity can aid in analyzing the
95 effects of erosion resulting from alterations in rainfall patterns due to climate change.

96 Various quality control (QC) methods for disdrometer data have been suggested to enhance the accuracy of derived
97 measurements (Kruger and Krajewski, 2002; Jaffrain and Berne, 2011; Raupach et al., 2015). QC approaches for
98 disdrometer data primarily rely on the falling velocity of raindrops. In the absence of a substantial wind influence or particle
99 collisions during descent, the fall velocity of a raindrop tends to increase with its diameter, ultimately reaching a terminal
100 velocity. Terminal velocity is achieved when the forces of air resistance and gravitational pull are in equilibrium, resulting in
101 no further particle acceleration (Wang and Pruppacher, 1977; Ong et al., 2021). Studies have been conducted to determine
102 the terminal velocities of raindrop particles (Atlas et al., 1973; Beard, 1977; Brandes et al., 2002), which have led to the
103 development of QC methods that use terminal velocity measurements. Kruger and Krajewski (2002) elucidated the structural
104 design and operational principles of a 2DVD system, and noted that the recorded data indicated a fall velocity of
105 approximately 400 m s^{-1} . However, this value is not feasible for raindrops. To mitigate the impact of erroneous data (outliers)
106 potentially arising from hardware malfunctions, inaccuracies in data processing, and environmental conditions at the
107 observation site, we employed a comparative analysis of the empirical relationship of raindrops established by Atlas et al.
108 (1973). Furthermore, recognizing that the disdrometer may either underestimate or overestimate the fall velocity of
109 precipitation particles influenced by the horizontal movement due to wind, this study conducted QC by focusing exclusively
110 on the vertical velocity measurements. Jaffrain and Berne (2011) conducted a study to address the uncertainties associated
111 with sampling observations from PARSIVEL disdrometers. They argued that the collected precipitation data exhibit inherent
112 variability and measurement errors attributable to the equipment used, necessitating the development of a method to mitigate
113 these issues and enhance data reliability. The authors proposed a method for eliminating anomalous data, such as outliers
114 (values that are not physically plausible), instances of particle splashing (where the same particle is detected multiple times),
115 and non-meteorological data. This preprocessing approach effectively diminished the sampling uncertainty of various
116 parameters, including rain rate.

117 Raupach et al. (2015) conducted a study using data from the PARSIVEL and 2DVD to establish a correction factor for
118 number concentration based on observations from the PARSIVEL disdrometer. The authors noted a tendency for
119 PARSIVEL to overestimate the number of small droplets measuring between 0.2 and 0.4 mm and larger particles measuring
120 2.4 mm or more. Furthermore, the measured fall velocity of larger droplets was lower than the actual terminal velocity.
121 Anomalous data can lead to DSD distortions, which can compromise the accuracy of precipitation measurements and radar-
122 based rainfall estimates. The focus of these studies was primarily on rainfall particles and it was determined that the
123 quantitative accuracy of rainfall estimates improved when the aforementioned QC methods were applied across various
124 environmental conditions.

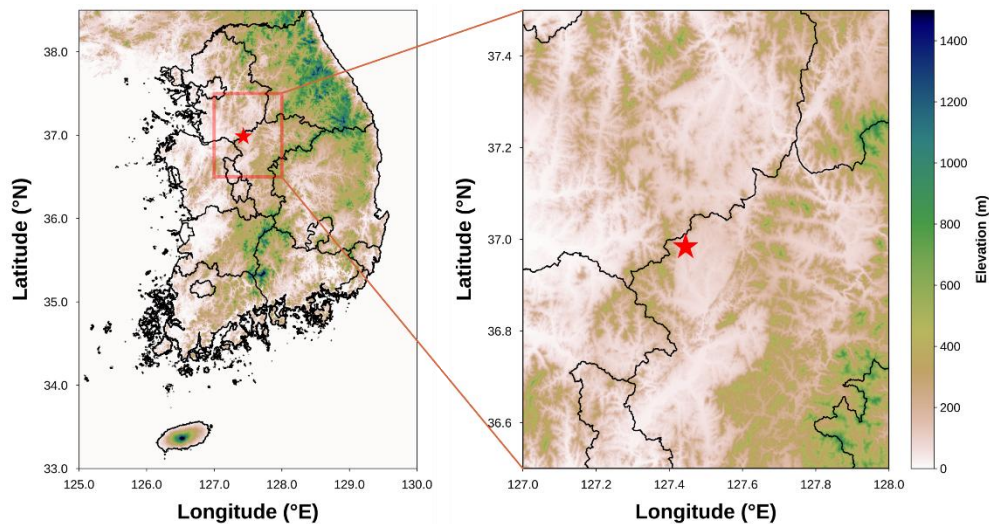
125 Snow particles exhibit a variety of forms such as needles, dendrites, and granules, which are influenced by temperature and
126 humidity. These variations in shape arise from the specific conditions under which the particles form and develop, leading to
127 differences in their densities and fall velocities (Barthazy and Schefold, 2006; Vázquez-Martín et al., 2021). Furthermore,

128 snow particles are more susceptible to wind because of their lower density and larger surface area than raindrops.
129 Consequently, fall-velocity-based QC methods for eliminating non-meteorological particles (such as leaves, dust, and insects)
130 are limited in their effectiveness because they primarily target solid particles with low fall velocities. Given the diverse
131 shapes and fall speeds of snow particles, the mixing of raindrops and snow during precipitation events may lead to an
132 underestimation of errors when applying conventional disdrometer QC methods. Therefore, it is imperative to establish
133 objective criteria for differentiating rainfall and snowfall conditions to enhance the accuracy of rainfall analysis using
134 disdrometer data. Ding et al. (2014) emphasized the significance of accurately classifying precipitation types for surface
135 energy balance and hydrological process research. They aimed to develop a method for identifying precipitation types by
136 analyzing 30 years of observational data. Their investigation focused on the correlation between precipitation type and
137 various meteorological variables, including wet-bulb temperature (T_w), relative humidity (RH), and surface elevation. These
138 findings indicate that using T_w as a reference variable for determining precipitation type is more reliable than relying on air
139 temperature (T_{air}). Furthermore, the proposed model, which incorporated T_w , demonstrated a determination accuracy
140 exceeding 88%.

141 This study aims to evaluate the quantitative accuracy of rainfall measurements obtained from a disdrometer in relation to
142 varying T_w conditions. Furthermore, this study seeks to establish environmental criteria to ensure the reliability of the
143 parameters used in the DSD model by using long-term rainfall data collected through disdrometer observations. A
144 comparative analysis of the disdrometer data was performed using different QC methods to examine the discrepancies
145 between these methods under varying T_w conditions.

146 **2 Data**

147 In this study, we evaluated the QC method applied to disdrometer data under varying precipitation conditions. To achieve
148 this, we collected and analyzed regional observational data that accounted for the environmental factors associated with
149 rainfall and snowfall. This study used data from a 2DVD installed at an observatory (Fig. 1) operated by the Weather Radar
150 Center of the Korea Meteorological Administration. The integrity of the 2DVD data was corroborated through comparisons
151 with measurements obtained from the tipping-bucket and weighing rain gauges. The analysis included observational data
152 collected between January 2020 and February 2024.



153 **Figure 1: Location of ground observation station.**

154 **2.1 Disdrometer**

155 The 2DVD (Kruger and Krajewski, 2002) used for the validity analysis of the disdrometer was an optical disdrometer
 156 developed by Joanneum Research. This instrument operates by projecting light through a bulb across a designated
 157 observation area and capturing the intensity of the transmitted light using a camera positioned on the opposite side (Fig. 2).
 158 When a particle, such as a raindrop, traverses the observation area (10 cm²) illuminated by the light sheet, its diameter is
 159 determined by analyzing the reduction in the intensity and width of the light during its passage. Furthermore, the system
 160 employs two cameras to observe the particles from orthogonal angles, allowing the fall velocity to be calculated based on the
 161 differential height of the light sheet in the two orientations and time taken for the particles to descend. The 2DVD's
 162 capability to acquire diameter and fall velocity data for individual particles offers superior temporal, dimensional, and
 163 velocity resolution compared to traditional disdrometer data, which typically provide channel-based information. The
 164 observational resolution of the camera was approximately 0.2 mm (512 pixels), making the particles smaller than the
 165 indistinguishable threshold (Grazioli et al., 2014). For quantitative validation using rain gauge data, the output time
 166 resolution was configured to one minute, with data classified at one-minute intervals.



167 **Figure 2: Two-dimensional video disdrometer.**

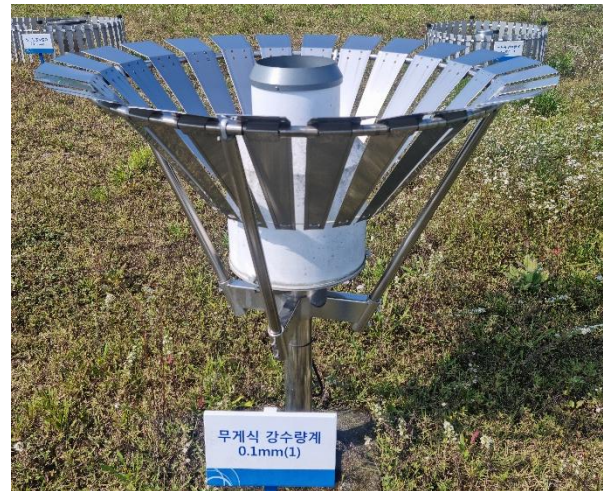
168 2.2 Rain gauge

169 Precipitation can occur in liquid droplets and solid particles, such as snow and graupel, when temperatures are at or near 0 °C.
 170 To validate the disdrometer data under T_w conditions, an analysis was conducted using data from the tipping-bucket and
 171 weighing-type rain gauges (Fig. 3). Each type of rain gauge offers an observational resolution of 0.1 mm and a temporal
 172 resolution of 1 min. Both instruments were positioned within a 10 m radius of the 2DVD disdrometer.

(a) Tipping-bucket type



(b) Weighing type



173 **Figure 3: (a) Tipping-bucket rain gauge (0.1 mm) and (b) Weighing rain gauge (0.1 mm).**

174 3 Methods

175 Ding et al. (2014) argued that precipitation types such as rain, snow, and sleet co-occur when the T_{air} or T_w approaches or
176 falls below 0 °C. They recommended using T_w as a more effective criterion for distinguishing between types of precipitation
177 instead of relying solely on T_{air} . In this study, the temporal resolution of the temperature data differed from that of previous
178 studies, which employed different temporal resolutions. To facilitate objective verification of the applicability of T_w , T_{air} and
179 T_w were employed as criteria for classifying precipitation types, and a comprehensive analysis was conducted.

180 3.1 Pre-processing of disdrometer data

181 A common QC approach for disdrometer data involves excluding non-meteorological data by analyzing fall velocity. In
182 numerous studies (Kruger and Krajewski, 2002; Jaffrain and Berne, 2011; Raupach and Berne, 2015; Kim et al., 2019), this
183 QC process was implemented by establishing a threshold determined by the terminal velocity, as indicated in Eq. (1).

$$|V_{measured} - V_{ideal}| < C \times V_{ideal} \quad (1)$$

184 where $V_{measured}$ and V_{ideal} represent the observed particle fall velocity (in m s^{-1}) and empirical fall velocity (or terminal
185 velocity), respectively. Constant C denotes the setting constant, which indicates the percentage of the terminal velocity. The
186 proportion of the removed particles may fluctuate based on the value of C . Numerous previous studies have provided
187 validation results using various setting constants. Studies that employed 2DVD data (Kruger and Krajewski, 2002; Thurai
188 and Bringi, 2005; Chang et al., 2009; Wen et al., 2018) predominantly adopted a setting constant of 0.4 (40%) during data
189 processing. Studies that employed PARSIVEL data for analysis frequently applied a setting constant of 0.6, accounting for
190 60% of the cases (Jaffrain and Berne, 2011; Friedrich et al., 2013; Ji et al., 2019; Kim et al., 2019). Given that previous
191 studies have encompassed various precipitation types, such as heavy rainfall, typhoons, orographic rainfall, and
192 thunderstorms, the established 40% and 60% QC conditions can be regarded as reliable preprocessing criteria for rainfall
193 events.

194 Raupach and Berne (2015) used data from a 2DVD instrument to derive correction factors for the drop-diameter channel in
195 the PARSIVEL dataset. The fall velocity filtering technique employed for the 2DVD and PARSIVEL data involved the
196 exclusion of particles exhibiting a terminal velocity exceeding 4 m s^{-1} , as shown in Eq. (2), those with a fall velocity below 3
197 m s^{-1} , as indicated in Eq. (3), and those larger than 7.5 mm , as shown in Eq. (4).

$$V_{measured} > V_{ideal} + 4 \quad (2)$$

$$V_{measured} > V_{ideal} - 3 \quad (3)$$

$$D > 7.5 \quad (4)$$

198 where D (in mm) is the diameter of the drop (or particle). This study involved a comparative analysis of the outcomes
199 derived from the three QC methods based on fall velocity. Terminal velocity was determined using the equation established
200 by Atlas et al. (1973) (Eq. (5)).

$$V_{ideal}(D) = 9.65 - 10.3\exp(-0.6D) \quad (5)$$

201 Three QC methods were used to evaluate the research findings. Methods 1 and 2 are used for the $\pm 40\%$ and $\pm 60\%$ ranges of
 202 terminal velocity, respectively, whereas Method 3 is based on the approach proposed by Raupach and Berne (2015).
 203 As the temperature decreased, various hydrometeors intermingled, resulting in a gradual reduction in the proportion of
 204 raindrops. Current QC methods are capable of eliminating low-density snow particles; however, to quantitatively compare
 205 and validate rainfall measurements obtained from rain gauge observations, particles that exhibit velocities below the
 206 threshold established for raindrops in each QC method are categorized as solid meteorological particles. In addition, analyses
 207 were conducted under the assumption that the solid particles melted and transformed into raindrops. This method aims to
 208 evaluate data from tipping-bucket rain gauges, which may exhibit diminished quantitative accuracy as the proportion of solid
 209 particles increases, and facilitate quantitative comparisons of rainfall observations derived from disdrometer data by
 210 implementing the QC method as the temperature decreases.

211 The equivalent-melted diameter (D_{eq}) at which a snow particle can transition into a raindrop while preserving its mass was
 212 determined using Eq. (6), established by Delanoë et al. (2005). In this equation, $\rho(D)$ (g cm^{-3}) denotes the density of snow
 213 particles as a function of their diameter, while ρ_w (g cm^{-3}) denotes the density of water. The density of the snow particles was
 214 computed based on the formula provided by Tiira et al. (2016) (Eq. (7)).

$$D_{eq} = \left(\rho(D) / \rho_w \right)^{1/3} D \quad (6)$$

$$\rho(D) = 0.226D^{-1.004} \quad (7)$$

215 3.2 Raindrop size distribution

216 The 2DVD data can be configured to correspond to user-defined diameter bin sizes, which in turn influence the
 217 characteristics of the DSD output and the precision of the DSD model parameters (Marzuki et al., 2010). Consequently, this
 218 study aims to facilitate the analysis of PASIVEL and 2DVD data for comparative purposes. To achieve this, 2DVD data
 219 were processed using the diameter channel information derived from the PASIVEL data to compute the rain rate, number
 220 concentration, and DSD model parameters. Detailed information regarding the diameter and velocity channels of the
 221 PASIVEL data is provided in the appendices (Table A3-4). The rain rate (R , mm h^{-1}) is calculated using Eq. (8), which
 222 incorporates the number concentration and fall velocity for each diameter. In determining the DSD model parameters after
 223 the rain rate calculation, data from intervals where the rain rate was 0.1 mm h^{-1} or greater were considered, thereby
 224 minimizing the uncertainty associated with the DSD model. The gamma model, recognized for its reliability in representing
 225 DSD characteristics, was selected for analysis. This model (Eq. (9)) is characterized by the shape parameter μ (Eq. (10)),
 226 slope parameter Λ (mm^{-1}) (Eq. (11)), and intercept parameter N_0 ($\text{mm}^{-1}\mu\text{m}^{-3}$) (Eq. (12)).

$$R = \frac{6\pi}{10^4} \int_{D_{min}}^{D_{max}} D^3 N(D) V(D) dD \quad (8)$$

$$N(D)_{gamma} = N_0 D^\mu \exp(-\Lambda D) \quad (9)$$

$$\mu = \frac{(7 - 11\eta) - [(7 - 11\eta)^2 - 4(\eta - 1)(30\eta - 12)]^{1/2}}{2(\eta - 1)} \quad (10)$$

$$\Lambda = \left[\frac{M_2 \Gamma(\mu + 5)}{M_4 \Gamma(\mu + 3)} \right]^{1/2} = \left[\frac{M_2(\mu + 4)(\mu + 3)}{M_4} \right]^{1/2} \quad (11)$$

$$N_0 = \frac{\Lambda^{(\mu+3)} M_2}{\Gamma(\mu + 3)} \quad (12)$$

227 The DSD parameters were derived from the n^{th} moment (M_n), as indicated in Eq. (13), along with the η value, computed
228 based on M_n as shown in Eq. (14).

$$M_n = \int_{D_{min}}^{D_{max}} D^n N(D) dD \quad (13)$$

$$\eta = \frac{\langle M_4 \rangle^2}{\langle M_2 \rangle \langle M_6 \rangle} = \frac{(\mu + 3)(\mu + 4)}{(\mu + 5)(\mu + 6)} \quad (14)$$

229 3.3 Wet-bulb temperature

230 Data from an Automatic Weather Station (AWS) installed at the observatory were used to compute the T_w . The T_{air} (in
231 degrees Celsius) and RH (in percentages) values derived from the AWS observations were incorporated into the T_w (in
232 degrees Celsius) calculation equation proposed by Stull (2011) (Eq. (15)) to determine the T_w value. The temporal resolution
233 of RH , T_{air} , and T_w was one minute, which was consistent with the temporal resolution of the disdrometer data.

$$T_w = T_{air} \operatorname{atan}\left[0.151977(RH + 8.313659)^{1/2}\right] + \operatorname{atan}(T_{air} + RH) - \operatorname{atan}(RH - 1.676331) \quad (15)$$

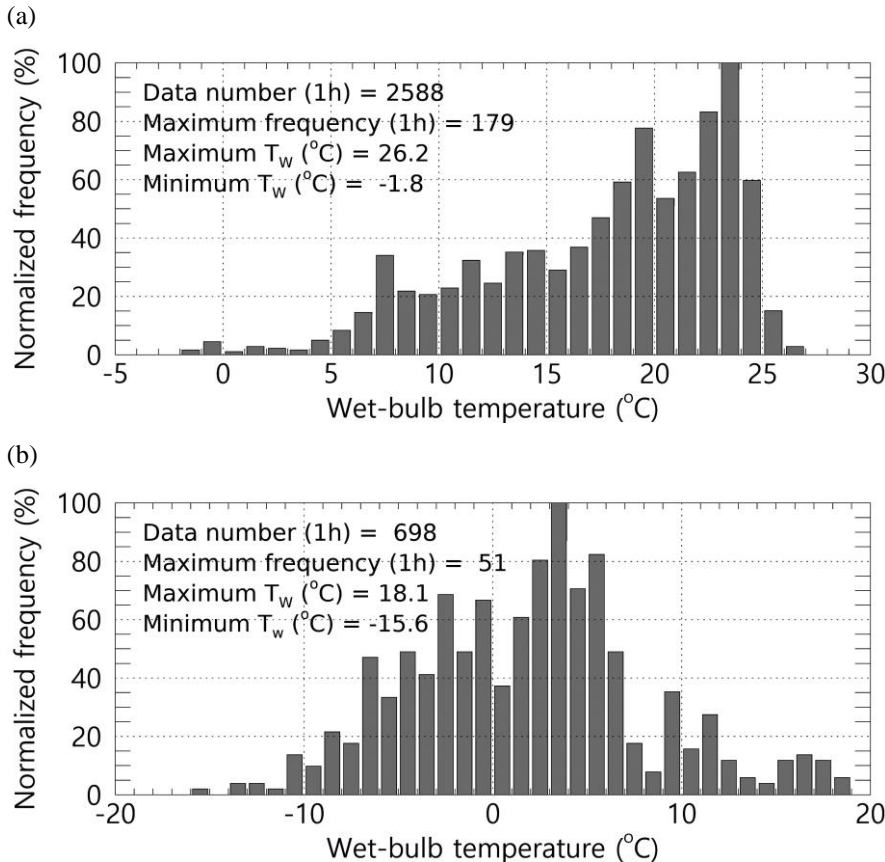
$$+ 0.00391838(RH)^{\frac{3}{2}} \operatorname{atan}(0.023101RH) - 4.686035$$

234 4 Results

235 4.1 Comparison of rainfall by the disdrometer pre-processing method

236 To validate the three QC methods employed for the disdrometer in this study, a comparative analysis was conducted between
237 the rainfall measurements obtained from the disdrometer and those recorded by rain gauges. This comparison utilizes hourly
238 accumulated rainfall data. Given that the QC methods for the disdrometer were specifically designed to address rainfall, the
239 variable T_w was employed to differentiate between rainfall and snowfall, thereby facilitating the verification of precipitation
240 type. Ding et al. (2014) argued that snow is infrequently detected when T_w exceeds 5 °C. Figure 4 shows the distribution of
241 T_w during the analysis period, specifically for instances when the hourly average T_w was either above or below 5 °C. An
242 examination of the one-minute T_w distribution during periods when the one-hour average T_w was 5 °C or higher (Fig. 4a)
243 revealed a maximum T_w of 26.2 °C, with the highest proportion of values exceeding 20 °C. Conversely, the proportion of
244 values falling below 5 °C was minimal, accounting for less than 5%. These findings suggest that it is feasible to delineate
245 rainfall periods using the hourly average T_w as a reference when comparing hourly accumulated rainfall values. In contrast,

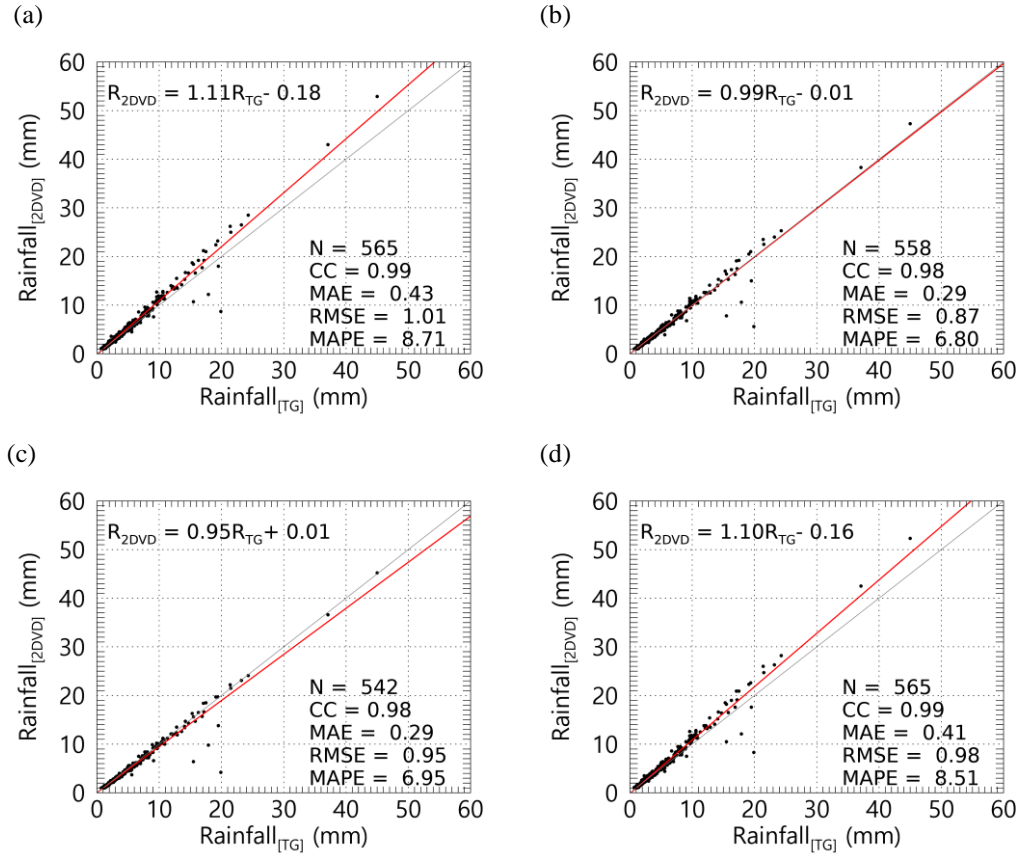
246 the distribution of one-minute T_w during hours when the average T_w was below 5 °C exhibited a broad range, with minimum
 247 and maximum T_w values exceeding 33 °C and a concentration of T_w values around 0 °C. This observation indicates notable
 248 variability in T_w under 5 °C or lower, suggesting that the observational area encompasses environmental conditions
 249 conducive to detecting diverse hydrometeors.



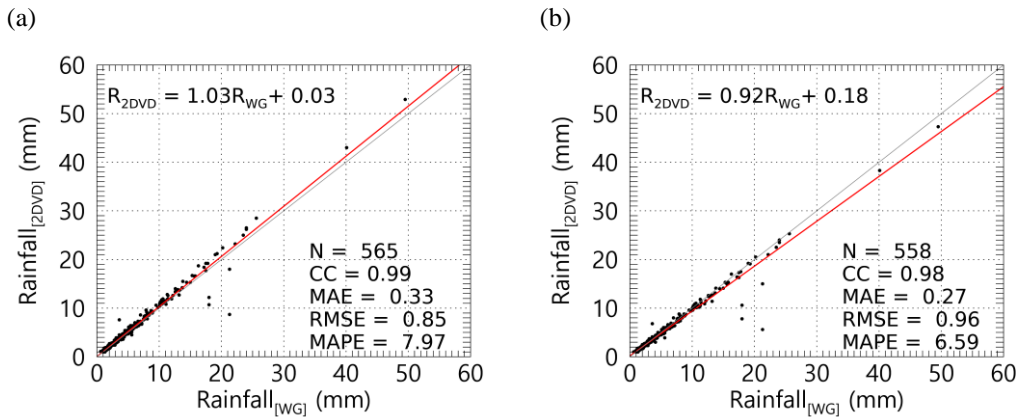
250 **Figure 4: Normalized frequency distribution of T_w during the analysis period (when the average hourly T_w is (a) $T_w \geq 5$ °C, (b) $T_w <$**
 251 **5 °C).**

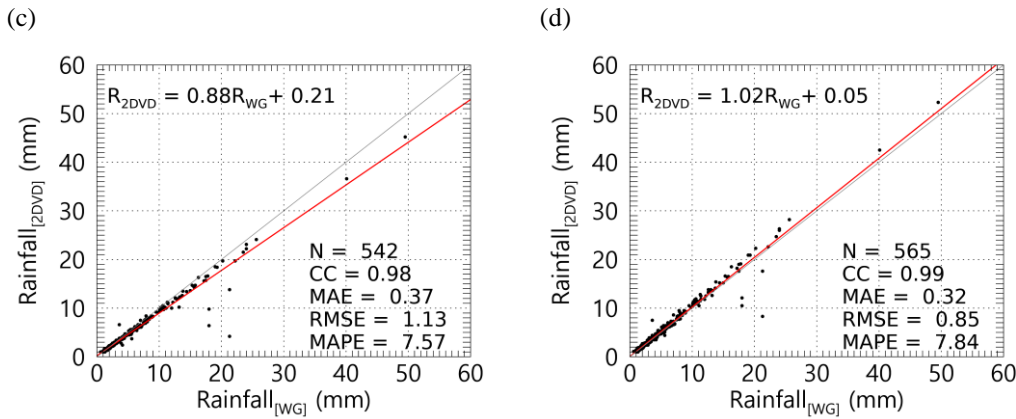
252 Figure 5-6 presents a comparative analysis of hourly rainfall measurements obtained from the tipping-bucket and weighing
 253 rain gauge, specifically under conditions where the temperature (T_w) equals or exceeds 5 °C, alongside data from the 2DVD
 254 observations. The results derived from the unprocessed raw data were analyzed to evaluate the impact of the QC procedures.
 255 The findings indicated a strong correlation, exceeding 0.98, between the 2DVD and rain gauge measurements, with a
 256 regression line slope of approximately unity. However, the raw data tended to overestimate the 2DVD-derived rainfall
 257 estimates compared to the QC-processed results. This discrepancy in the overestimation of the 2DVD data can be attributed
 258 to variations in the conditions under which particles are eliminated, which is contingent on the specific QC method
 259 employed. Following the application of the QC methods, the mean absolute percentage error (MAPE) demonstrated an

260 overall reduction compared with the raw data, suggesting that all QC methods possess quantitative reliability for rainfall data,
 261 with a maximum reduction of approximately 2.1%.



262 **Figure 5: Comparison of rainfall observed using the tipping-bucket rain gauge and 2DVD when $T_w \geq 5$ °C ((a) Unfiltered, (b)**
 263 **Method 1, (c) Method 2, (d) Method 3). R_{2DVD} and R_{TG} denote the rainfall obtained from the 2DVD and a tipping-bucket rain**
 264 **gauge, respectively.**





265 **Figure 6: Comparison of rainfall observed using the weighing rain gauge and 2DVD when $T_w \geq 5^\circ\text{C}$ ((a) Unfiltered, (b) Method 1,**
 266 **(c) Method 2, (d) Method 3). R_{WG} denotes the rainfall obtained from a weighing rain gauge.**

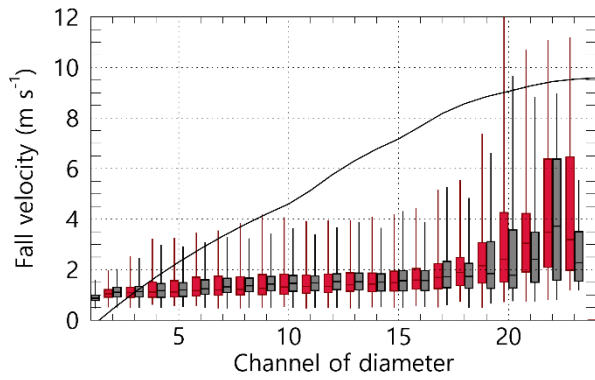
267 4.2 Fall velocity of particle by temperature and wet-bulb temperature

268 4.2.1 Fall velocity distribution at T_{air} and T_w

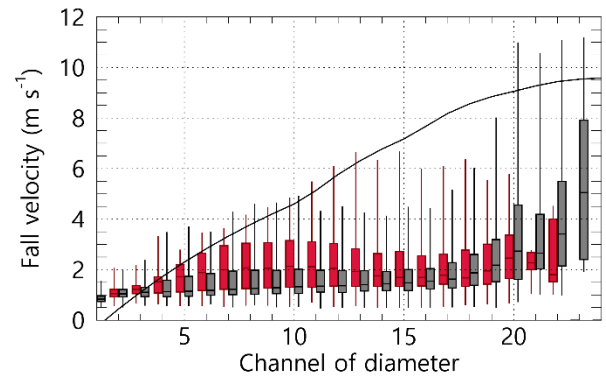
269 Figure 7 shows the distribution of the fall velocity with the diameter of precipitation particles (raindrops) under varying
 270 conditions of T_w and T_{air} . When the T_w and T_{air} ranged from -1 to 0°C , the fall velocity distributions were relatively
 271 comparable. However, as the temperature exceeded 0°C , the fall velocity for CH 4 to 18 increased under T_w conditions,
 272 while under the T_{air} condition, it exhibited values similar to those observed at temperatures below 0°C (Fig. 7(a-b)). When
 273 T_w was below 0°C , the upper 75% value of fall velocity was less than 2 m s^{-1} . However, as T_w increased above 0°C , fall
 274 velocity increased to approximately 1 m s^{-1} or higher in the CH4–15 diameter range. Particularly in the CH8–11 range, the
 275 upper 75% value exceeded 3 m s^{-1} . Specifically, up to CH13, the fall velocity gradually increased with diameter, reaching
 276 large values exceeding 6 m s^{-1} . Conversely, under T_{air} conditions, the upper 75% fall velocity values for the CH1–15 range
 277 were 2 m s^{-1} or less in the 0 – 1°C range. Under T_{air} conditions, the fall velocity increased when the temperature was above
 278 1°C . Notably, when the temperature rose above 1°C , there was a notable increase in fall velocity; under T_w conditions, the
 279 distribution approached the terminal velocity of raindrops. Conversely, for diameters in the CH 12 or a higher range, the fall
 280 velocity remained at approximately 5.5 m s^{-1} despite increases in diameter. Under T_{air} conditions, the fall velocity increased
 281 when temperatures were above 1°C . However, it remained lower than that observed under T_w conditions, with a broader
 282 distribution of fall velocities across the diameter channels (Fig. 7(c)). At 2°C or higher temperatures, T_w and T_{air} conditions
 283 yielded fall velocity distributions that were close to the terminal velocity of raindrops, with an increasing trend in
 284 distribution as temperature increased (Fig. 7(d-f)). However, under T_{air} conditions, the fall velocity was notably low,
 285 remaining below 2 m s^{-1} for diameters of 3 mm (CH 17) or larger.

(a) $-1^\circ\text{C} \leq T_w (T_{air}) < 0^\circ\text{C}$

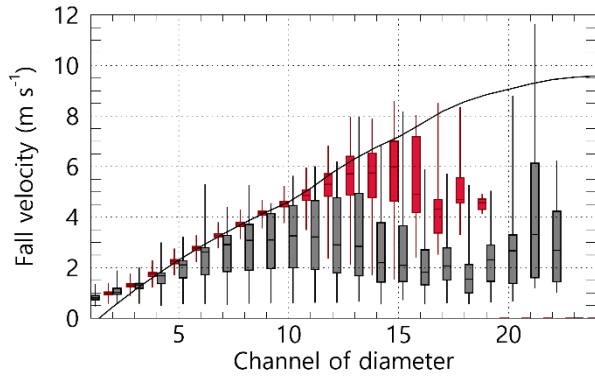
(b) $0^\circ\text{C} \leq T_w (T_{air}) < 1^\circ\text{C}$



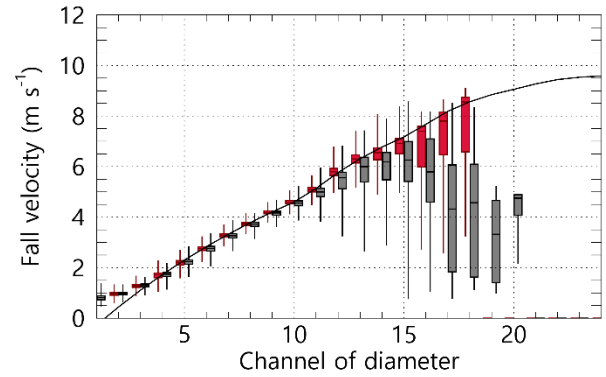
(c) $1\text{ }^{\circ}\text{C} \leq T_w (T_{air}) < 2\text{ }^{\circ}\text{C}$



(d) $2\text{ }^{\circ}\text{C} \leq T_w (T_{air}) < 3\text{ }^{\circ}\text{C}$



(e) $3\text{ }^{\circ}\text{C} \leq T_w (T_{air}) < 4\text{ }^{\circ}\text{C}$

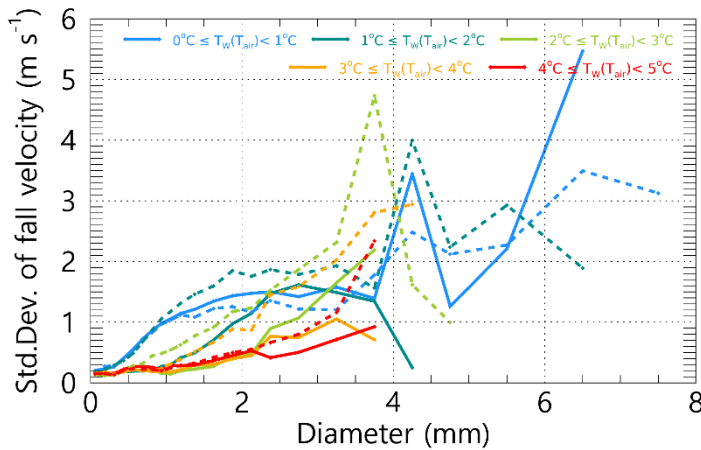


(f) $4\text{ }^{\circ}\text{C} \leq T_w (T_{air}) < 5\text{ }^{\circ}\text{C}$

286 **Figure 7: Distribution of fall velocity by diameter channel based on T_w (red) and T_{air} (gray). The black solid line represents the**
 287 **terminal velocity of rain drops proposed by Atlas et al. (1973).**

288 Figure 8 shows the variability in fall velocity with respect to the changes in temperature. Notably, despite T_w and T_{air}
 289 exhibiting similar numerical ranges, the distribution of fall velocity was considerably broader under T_{air} conditions. When T_w
 290 exceeds $3\text{ }^{\circ}\text{C}$, the standard deviation across all diameter intervals remains low, approximately 1 m s^{-1} or less. In instances
 291 where T_w ranges between 2 and $3\text{ }^{\circ}\text{C}$, an increase in distribution is observed for diameters of 2.5 mm or greater, while the

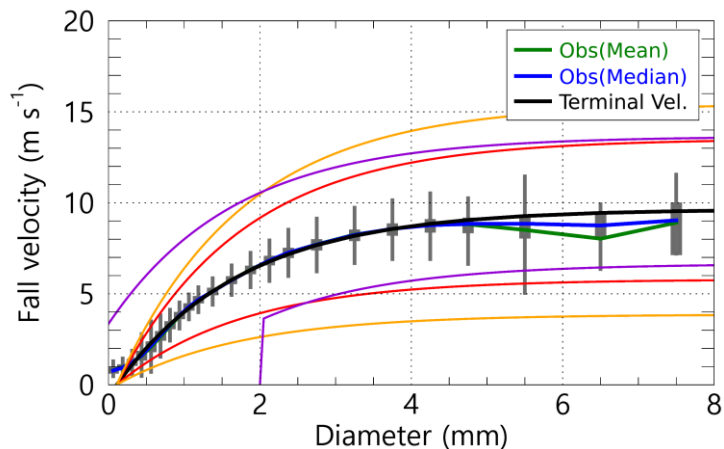
292 standard deviation for diameters of 1 mm or more increases when T_w is between 1 and 2 °C. As temperature decreased, the
 293 range of diameters exhibiting increased fall velocity variability progressively expanded. According to the findings under T_{air}
 294 conditions, the standard deviation of fall velocity for diameters exceeding 1 mm begins to rise below 4 °C, with values
 295 surpassing 1 m s⁻¹ for diameters greater than 2 mm. The observation that when T_{air} is between 2 and 3 °C, the standard
 296 deviation of fall velocity for diameters ranging from 3 to 4 mm is considerably increased, exceeding 2 m s⁻¹ and reaching up
 297 to 4.5 m s⁻¹ is noteworthy. This broad fall velocity distribution suggests a mixture of various hydrometeors, complicating the
 298 differentiation between rain and snow based solely on fall velocity. Consequently, subsequent analyses were conducted
 299 using T_w as the criterion for distinguishing between rain and snow.



300 **Figure 8: Standard deviation of fall velocity by T_w (solid line) and T_{air} (dash line) range (1 °C interval).**

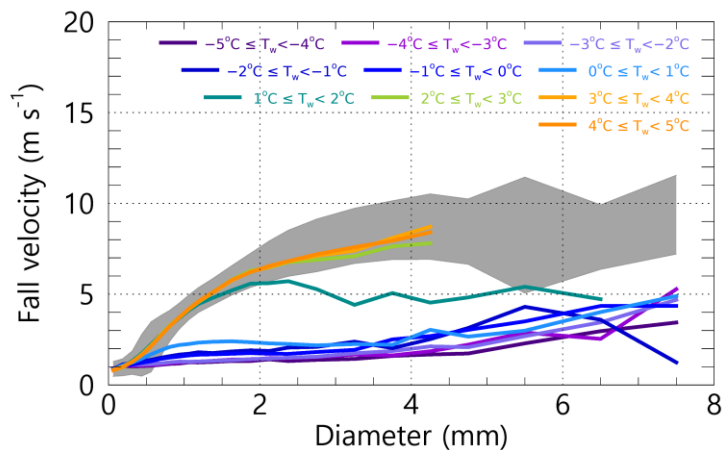
301 4.2.2 Fall velocity distribution under rainfall condition

302 Figure 9 shows the distribution of fall velocities by diameter, derived from data collected when the T_w was at or above 5 °C.
 303 The central value of the fall velocity is consistent with the terminal velocity. This is within the range of fall velocities for
 304 raindrops, as established by the three different QC methods based on the fall velocity. It is important to note that
 305 precipitation particles (drops) may experience variations in their fall velocities owing to factors such as wind influence or
 306 collisions with obstacles during descent. The findings presented in Fig. 9 suggest that the observatory's measurements were
 307 not considerably affected by wind or obstacles, thereby confirming the reliability of the velocity observation data of the
 308 disdrometer.



309 **Figure 9: Distribution of fall speed by diameter under conditions of $T_w \geq 5$ °C, and effective fall velocity of raindrops by pre-**
 310 **processing methods (The red (method 1), orange (method 2), and purple (method 3) solid lines represent the effective velocity of**
 311 **raindrop applied to each QC method).**

312 An analysis of the fall velocity corresponding to temperature intervals (T_w) of 1 °C revealed that when T_w is at or above 2 °C,
 313 the fall velocities correspond with those typically observed for raindrops. Conversely, at T_w values between 1°C and 2 °C,
 314 particles with diameters of 2 mm or less fall within the raindrop velocity range; however, as the diameter increases to 2 mm
 315 or more, the fall velocity diminishes, stabilizing at approximately 5 m s⁻¹. Temperature conditions (T_w) may indicate a
 316 mixture of raindrops and snow particles. At temperatures below 1 °C, the fall velocity of droplets with diameters of 4 mm or
 317 less decrease to approximately 3 m s⁻¹, exhibiting a low-velocity distribution of 5 m s⁻¹ or less across all diameter ranges.
 318 This distribution suggests a higher proportion of solid (snow) particles when T_w is less than 1 °C.



319 **Figure 10: Distribution of fall velocity by diameter in each T_w range. The grey area in the figure represents the Q1 (25%) – Q3**
 320 **(75%) for the fall velocity by diameter when $T_w \geq 5$ °C.**

321 4.3 Accuracy of quantitative rainfall by wet-bulb temperature

322 Figures 11 and 12 show the outcomes of the comparative analysis and validation of rainfall measurements derived from the
323 QC method applied to each T_w range, juxtaposed with the rainfall values obtained from a rain gauge. Figure 11 shows the
324 results of applying the QC method, which effectively filtered out all particles except for raindrops. In contrast, Fig. 12
325 depicts the assumption that the particles exhibiting low fall velocities are snow that melts and transforms into raindrops. The
326 verification metrics employed in this analysis included the Root Mean Square Error (RMSE), Mean Absolute Error (MAE),
327 MAPE, Correlation Coefficient (CC), slope (a_1), and intercept (a_0) derived from Eq. (14), which is the first-order regression
328 equation correlating rainfall measurements from the rain gauge and 2DVD.

$$R_{2DVD} = a_1 R_{Gauge} + a_0 \quad (14)$$

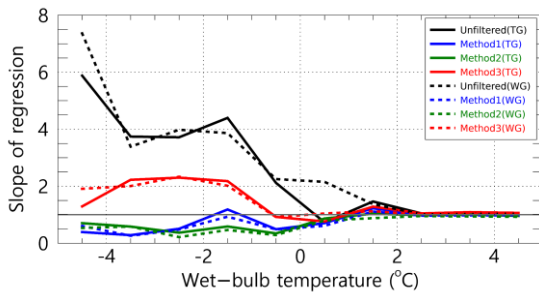
329 The a_1 of the observed relationship indicates that when the T_w exceeds 2 °C, the value remains close to one before and
330 following the application of QC. However, as T_w drops below 2 °C, the value of a_1 either increases or decreases. A value of
331 a_1 greater than one suggests that the rainfall measurements derived from the 2DVD instrument tend to overestimate the
332 corresponding values obtained from the rain gauge observations. In contrast, a value of less than one indicates an
333 underestimation. Notably, in the absence of QC, a_1 increases to two or more at temperatures below 0 °C, with the extent of
334 overestimation intensifying as T_w decreases. This phenomenon is particularly evident when validated against a tipping-
335 bucket rain gauge, where values of two or greater were recorded at temperatures ranging from 0 to 1 °C. This observation
336 may be attributed to the different operational principles of the various rain gauge types within the specified T_w range (Fig.
337 11a). At T_w below 0 °C, the unfiltered data and Method 3 exhibit a_0 values exceeding one, while Method 2 and Method 3
338 present a_1 values below one. This discrepancy can be interpreted as a consequence of the varying quantities of preprocessed
339 particles. For T_w values of 1 °C or higher, a_0 is observed to range between 0 and 1; however, as T_w declines below 1 °C, a_0
340 experiences a rapid increase. Method 3, which uses a smaller filter area for unfiltered particles and those with diameters of 2
341 mm or less, demonstrates a_0 values of 0.2 or higher, exceeding those of Methods 1 and 2 (Fig. 11b).

342 The CC decreases substantially in the T_w range, whereas a_0 increases considerably (Fig. 11f). The RMSE and MAE were
343 recorded at low values of less than 0.3 mm and 0.2 mm, respectively, when T_w was at or above 2 °C; however, these errors
344 increased as T_w decreased to 1 °C or lower, with the magnitude of errors following the order of Unfiltered, Method 3,
345 Method 1, and Method 2, which corresponds to the increasing trend of a_1 . In the range of 0 to 2 °C, the errors associated with
346 results validated by the tipping-bucket rain gauge were greater than those from the weighing rain gauge (Fig. 11(c-d)). The
347 MAPE exhibited its lowest error rate, below 20%, at temperatures between 3 and 4 °C. It progressively increased with a
348 decrease in T_w , ultimately reaching values of approximately 30% or more at temperatures of 2 °C or lower.

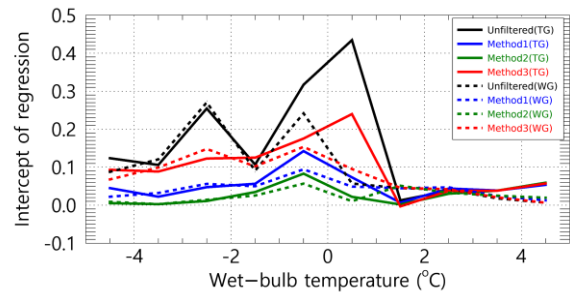
349 Comparable findings were observed when it was assumed that the snow particles melted (Fig. 12), with an increase in error
350 as the temperature (T_w) dropped below 2 °C. The distinction between melted and unmelted snow particles was demonstrated
351 using a weighing rain gauge as a verification tool. In scenarios where the melted state was disregarded at T_w values lower
352 than 2 °C, the variability in the MAPE and CC was substantial, which was contingent upon fluctuations in T_w . Conversely,

353 the variability decreased when the melted state was considered, and the CC remained elevated approximately at 0.8 or above.
 354 The pronounced escalation in error within the 0–1 °C range can be attributed to precipitation detected by the 2DVD system
 355 that was not captured by the Tipping-bucket rain gauge (Fig. A1(f) in Appendix).
 356 Furthermore, the low volatility and high correlation observed in the verification results using the weighing rain gauge within
 357 the T_w range can be explained by incorporating raindrops and snow particles in the 0–1 °C range. By assuming melting of
 358 snow particles, both forms of precipitation can be integrated into precipitation calculations. The weighing rain gauge
 359 recorded precipitation values that accounted for the cumulative weight of all the raindrops and snow particles (Fig. A2(f) in
 360 the Appendix).

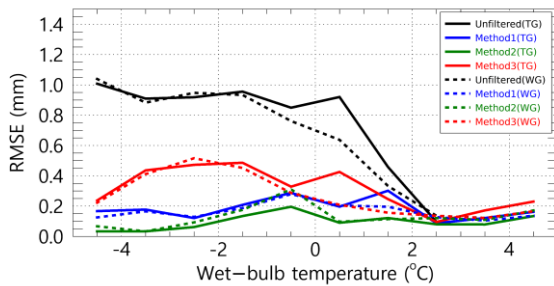
(a) a1



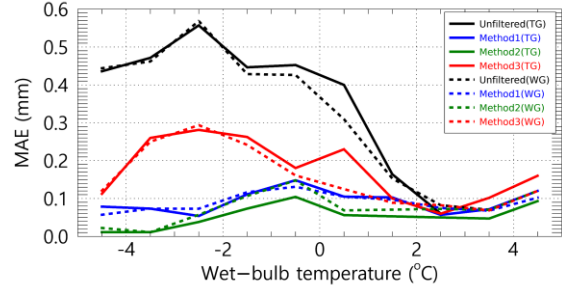
(b) a0



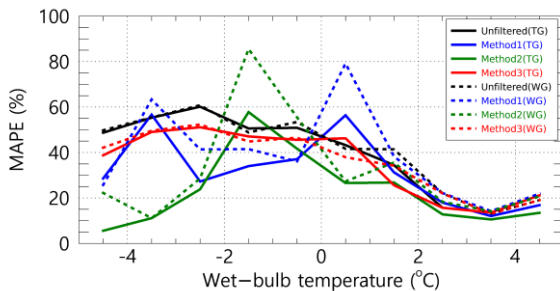
(c) RMSE



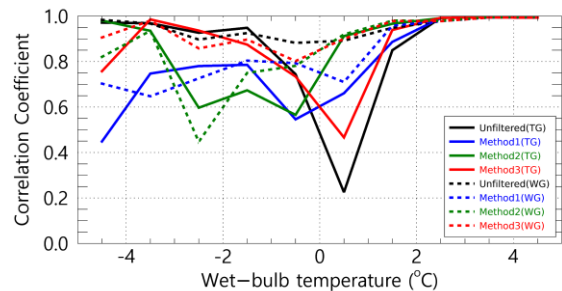
(d) MAE



(e) MAPE

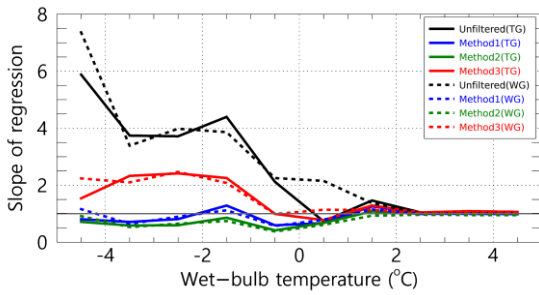


(f) CC

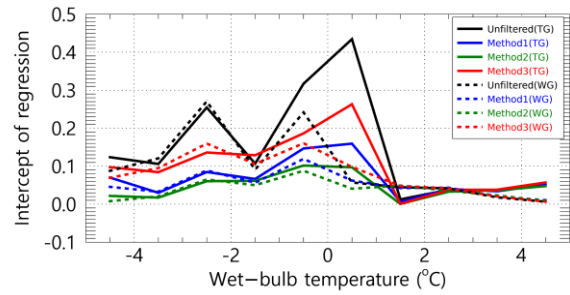


361 **Figure 11: Quantitative comparison of rainfall from a rain gauge (The solid line represents the tipping-bucket and the dash line**
 362 **represents the weighing rain gauge) and 2DVD by T_w (assuming that snow particles do not melt).**

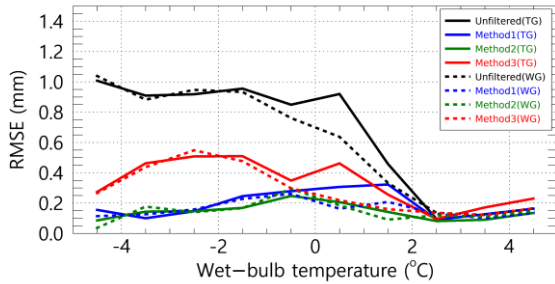
(a) a1



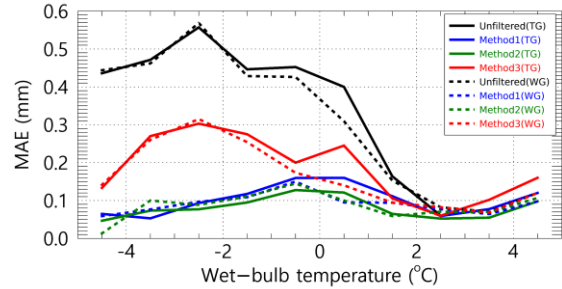
(b) a0



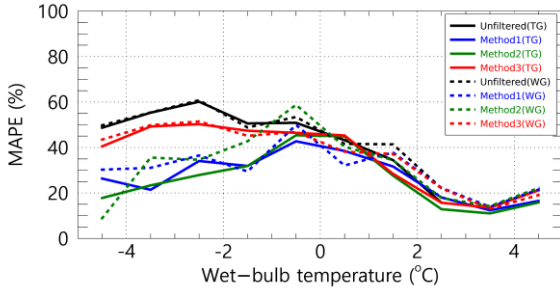
(c) RMSE



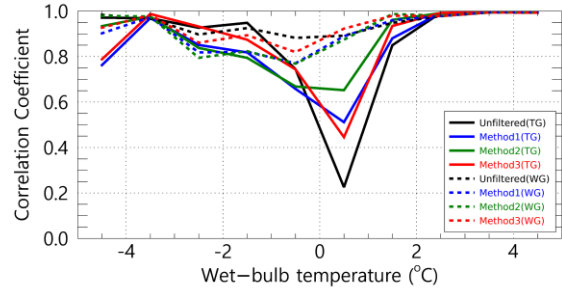
(d) MAE



(e) MAPE



(f) CC



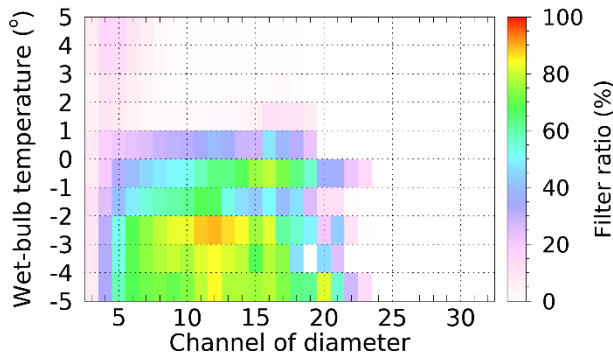
363 Figure 12: Quantitative comparison of rainfall from a rain gauge (The solid line represents the tipping-bucket and the dash line
364 represents the weighing rain gauge) and 2DVD by T_w (assuming that snow particles melt).

365 4.4 Particle filter rate

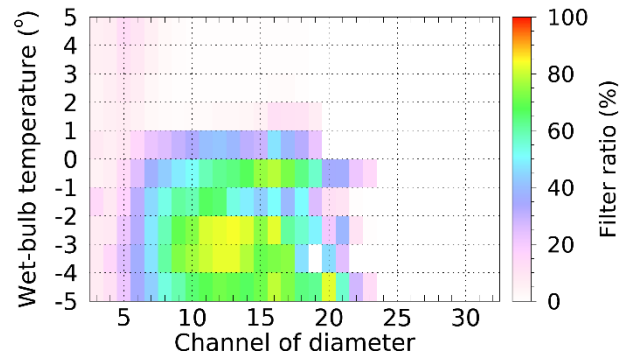
366 Precipitation measurements obtained from the disdrometer were derived from raindrop (or snow particle) accumulation. The
367 quantitative errors associated with these precipitation measurements were assessed by comparing the filter rates of raindrops
368 (or snow particles) using the QC method. Figure 13 shows the filter ratios corresponding to the T_w range and channel
369 diameter. The two methods, Method 1 and Method 2, exhibit differences in the range of removal velocities based on particle
370 diameter (see Fig. 9); specifically, Method 2 encompasses a broader spectrum of raindrop sizes compared to Method 1,
371 leading to an increased filter rate when the T_w is below 0 °C. Notably, the filter rate for Method 2 surpasses that of Method 1
372 at temperatures lower than -2 °C. Conversely, Method 3 did not allow the removal of particles smaller than 2 mm (as

373 indicated in CH 14), regardless of their low fall velocity, resulting in a consistent filter rate of 0%, irrespective of variations
 374 in T_w . This suggests that the number of particles smaller than 2 mm may be greater in Methods 1 and 2. Furthermore, the
 375 filter rate was lower when snow particles were assumed to have melted than when they had not melted. Nonetheless, for
 376 particles with a diameter of 1 mm or less, the filter rate ranged from approximately 10% to 30% when T_w exceeded 1 °C,
 377 which appears to be attributable to the removal of particles exhibiting a fall velocity that exceeds the raindrops.

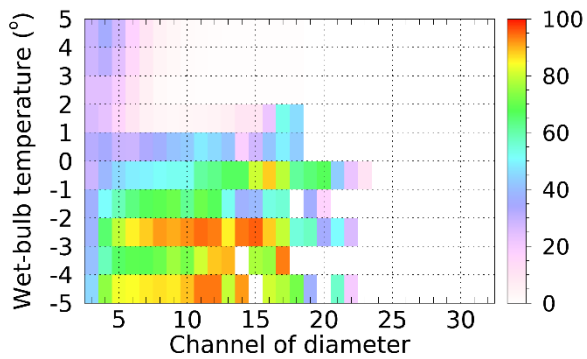
(a) Method 1



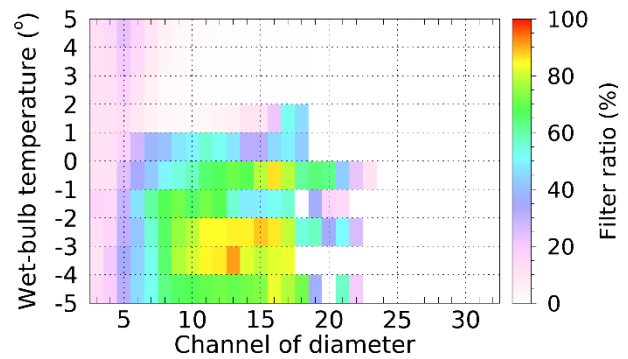
(b) Method 1 (melted)



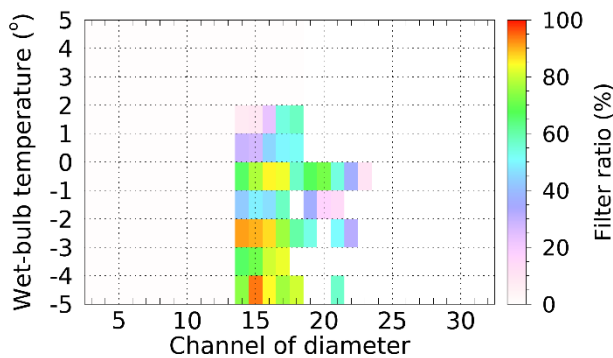
(c) Method 2



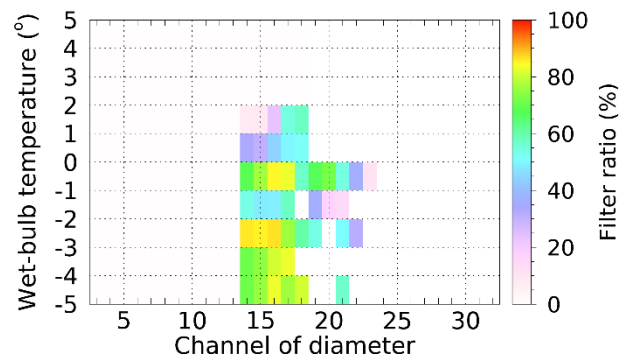
(d) Method 2 (melted)



(e) Method 3



(f) Method 3 (melted)



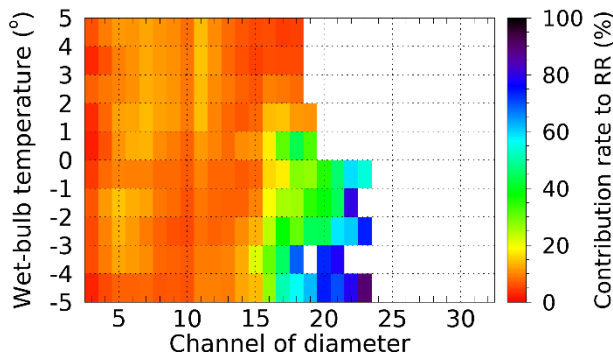
378 **Figure 13: Particle filter ratio by diameter channel for T_w according to the pre-processing method based on falling velocity.**

379 4.5 Contribution rate by particle diameter to precipitation intensity

380 Figure 14 shows the contribution rate of the number concentration by diameter to the precipitation intensity as derived from
381 the disdrometer data. It is observed that when the T_w exceeds 1 °C, the contribution rate remains approximately 20% or lower
382 across all diameters. Conversely, when T_w is below 1 °C, the concentration of particles measuring 3 mm (CH 15) or larger
383 considerably influences the calculation of precipitation intensity. The contribution rate of 1.25 to 1.75 mm diameter (CH 11
384 to 13) decreased when the temperature was lower than 1 °C. The decrease in the contribution rate of drops smaller than 3
385 mm and the increase in the contribution rate of larger drops was as a result of the decrease in the concentration of drops
386 smaller than 3 mm through the QC process (Section 4.4), which increased the impact of relatively larger drops on the
387 calculation of precipitation intensity. This phenomenon can be attributed to the direct proportionality of the precipitation
388 intensity to $N(D)$ and D^3 , indicating that an increase in the particle diameter substantially affected the results. After QC, a
389 substantial increase in the contribution rate for a specific diameter may affect the precipitation intensity owing to a decrease
390 in the concentration of drops in the diameter range with a lower contribution rate.

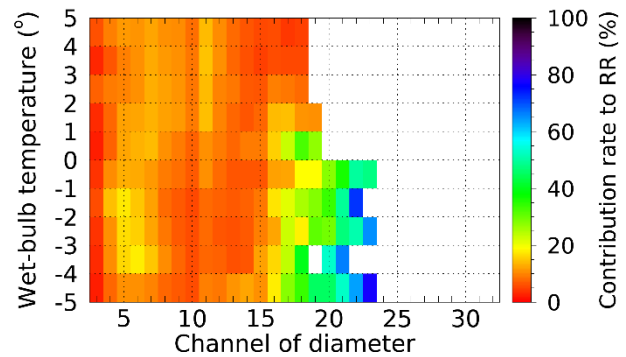
391 In scenarios where it is assumed that snow particles have melted, the diameter of these particles decreases, increasing the
392 concentration of smaller particles. As a result, the contribution rate of diameter from approximately 0.5 to 1 mm (CH 5 to 10)
393 increased. Notably, in Method 3, there was a minimal removal of particles smaller than 2 mm, which resulted in negligible
394 differences between the scenarios that accounted for the melted state of snow particles and those that did not.

(a) Method 1

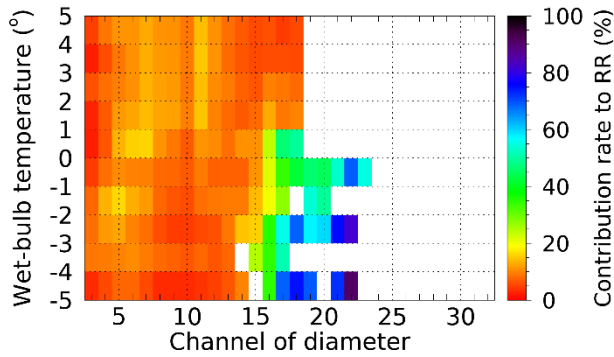


(c) Method 2

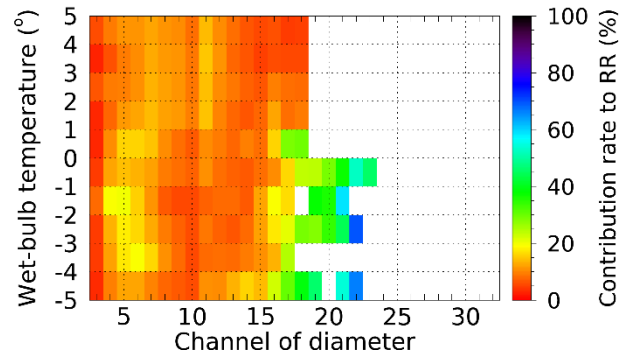
(b) Method 1 (melted)



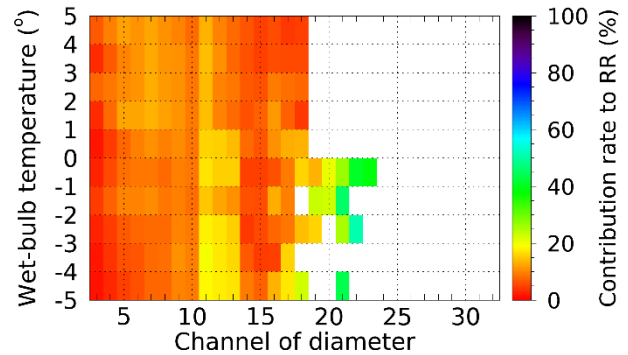
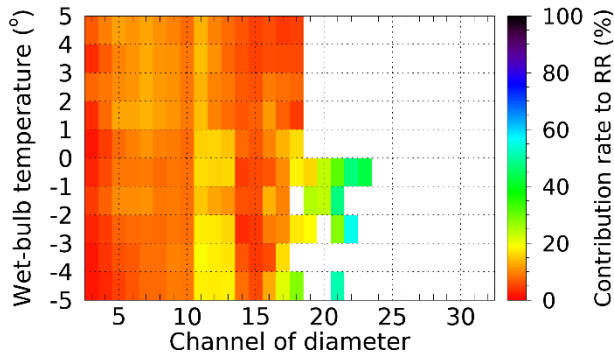
(d) Method 2 (melted)



(e) Method 3



(f) Method 3 (melted)



395 **Figure 14: Precipitation contribution rate by diameter channel for T_w using the pre-processing method based on falling velocity.**

396 4.6 Drop size distribution

397 4.6.1 Number concentration calculated by applying QC methods based on T_w

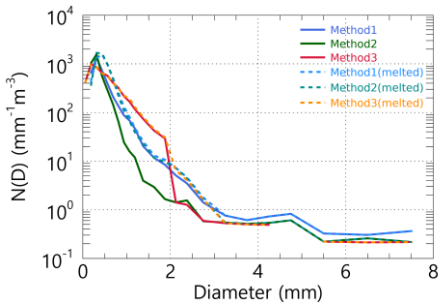
398 The precipitation intensity derived from disdrometer data is contingent on the number concentration; therefore, examining
 399 the distribution of the number concentration is imperative. Figure 15 shows the average distribution of the number
 400 concentration obtained by applying the QC method under varying T_w conditions. Notably, when the temperature exceeded
 401 2 °C, the distributions yielded by all QC methods were comparable. Method 3 exhibited a relatively high concentration of
 402 small droplets measuring 1 mm or less, whereas the number of droplets measuring 1 mm or more showed minimal variation
 403 (Fig. 15h). This finding indicates that, at temperatures above 2 °C, the output values remain consistent across different QC
 404 methods.

405 At temperatures ranging from 1 to 2 °C, the distribution of particles exceeding 2 mm in size was distinctly differentiated
 406 according to the QC method employed. This finding suggests that the fall velocity of particles larger than 2 mm exhibits
 407 considerable variation within this temperature interval (Fig. 10). Conversely, at temperatures below 1 °C, the distribution
 408 obtained through Method 3 displayed an anomalous pattern. This irregularity can be attributed to the failure of Method 3 to
 409 exclude snow particles smaller than 2 mm, leading to a higher concentration than that of the other QC methods. When

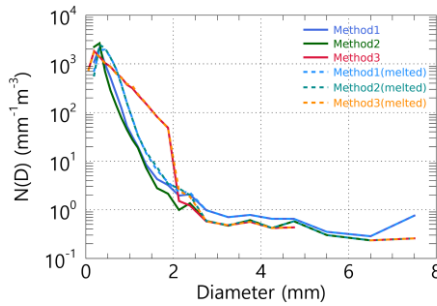
410 considering the scenario in which particles are assumed to have melted, an increase in the concentration of water was
 411 observed for particles with a diameter of 1 mm or less when the T_w was between 0 and 1 °C, while the concentration of
 412 particles larger than 2 mm remained relatively unchanged.

413 In comparing scenarios where particles are assumed to have melted versus those that are not, no notable differences were
 414 observed at temperatures exceeding 1 °C (see Fig. 15g). However, within the temperature range of 0 to 1°C, there was an
 415 increase in the number of particles smaller than 1 mm. There was a similar distribution in the number of medium and larger
 416 particles (1 mm or more). As the T_w progressively decreased below 0 °C, the disparity in the number concentration of
 417 particles larger than 1 mm became more pronounced (Fig. 15(a-e)).

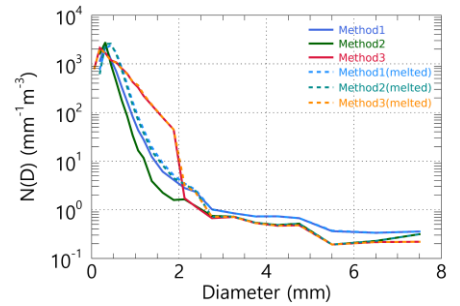
(a) $-5\text{ °C} \leq T_w < -4\text{ °C}$



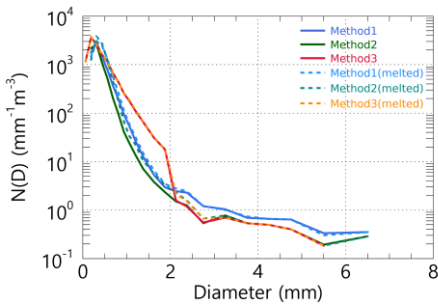
(b) $-4\text{ °C} \leq T_w < -3\text{ °C}$



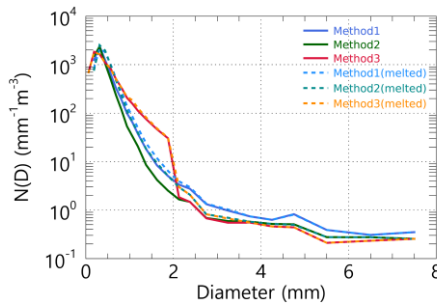
(c) $-3\text{ °C} \leq T_w < -2\text{ °C}$



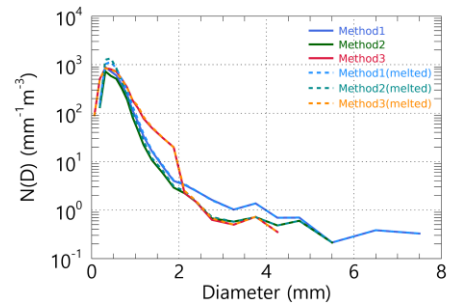
(d) $-2\text{ °C} \leq T_w < -1\text{ °C}$



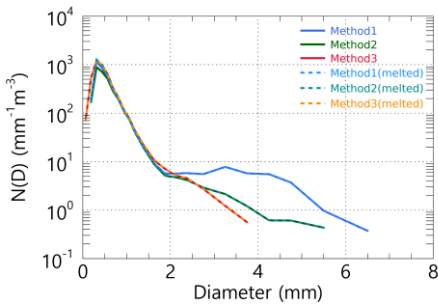
(e) $-1\text{ °C} \leq T_w < 0\text{ °C}$



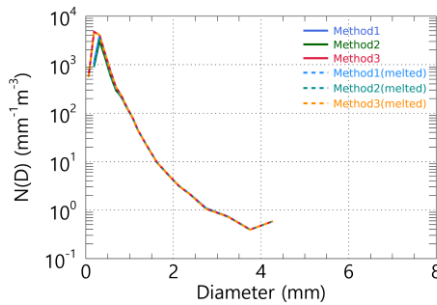
(f) $0\text{ °C} \leq T_w < 1\text{ °C}$



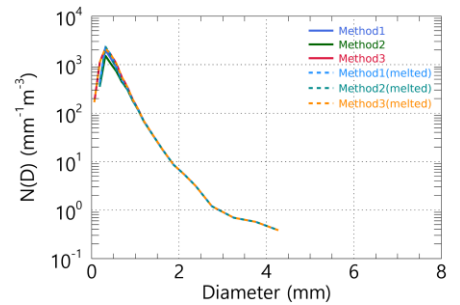
(g) $1\text{ °C} \leq T_w < 2\text{ °C}$



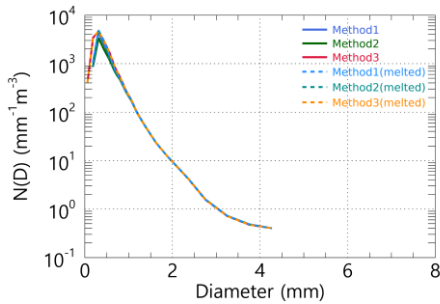
(h) $2\text{ °C} \leq T_w < 3\text{ °C}$



(i) $3\text{ °C} \leq T_w < 4\text{ °C}$



(j) $4\text{ °C} \leq T_w < 5\text{ °C}$



418 **Figure 15: Average number concentration distribution for T_w using pre-processing methods.**

419 **4.6.2 Difference in the number concentration based on the gamma model**

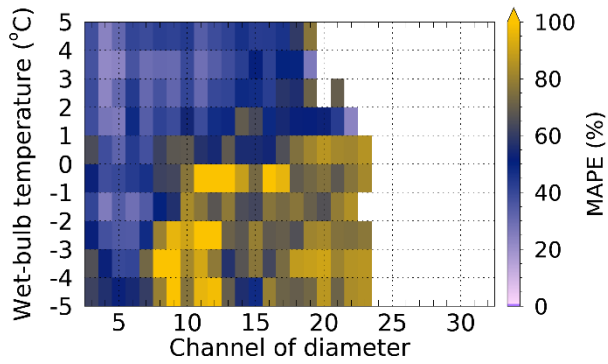
420 The change in the shape of the number concentration within the observed data has implications for DSD model parameters.
 421 The notable discrepancy between the observed number concentration and that derived from the model parameters raises
 422 concerns regarding the reliability of the DSD model.

423 Figures 16 and 17 show the variance between the observed number concentration and that predicted using the gamma model.
 424 When all QC methods were implemented, the MAPE remained below 60% across all diameter ranges at temperatures
 425 exceeding 2 °C. However, as the T_w fell below 1 °C, the discrepancy for diameters greater than 0.6 mm (CH 7) escalated to
 426 over 70%. At 2 °C or higher temperatures, the gamma distribution overestimated the concentration of particles smaller than 1
 427 mm while underestimating those larger than 1 mm. Nonetheless, the extent of under- or over-simulation by gamma
 428 distribution remained below 50% across all diameter intervals.

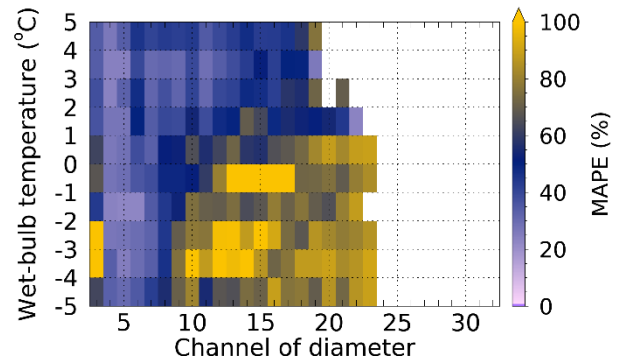
429 When T_w was below 1 °C, assuming that the snow particles had melted, the error rate in simulating the concentration of
 430 particles smaller than 1 mm (CH 8) diminished (Fig. 16(b, d)). Concurrently, the percentage bias (PBAS) for particle
 431 diameters less than 1 mm decreased, approaching a value near zero (Fig. 17(b, d)). This phenomenon can be attributed to the
 432 application of the QC method under subzero conditions, which led to an overestimation of the gamma distribution for
 433 diameters of 1 mm or less because of the increased influence of smaller particles resulting from the exclusion of larger
 434 particles exceeding 3 mm. Conversely, this resulted in an underestimation of the gamma distribution for diameters larger
 435 than 3 mm.

(a) Method 1

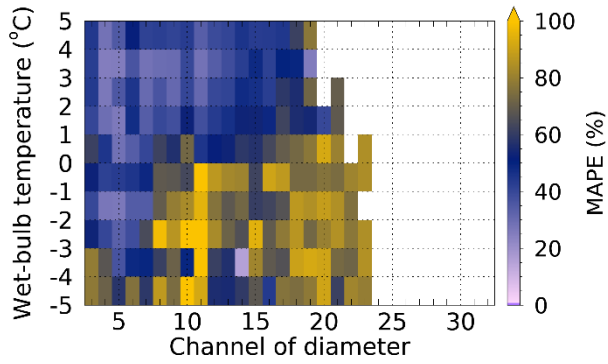
(b) Method 1 (melted)



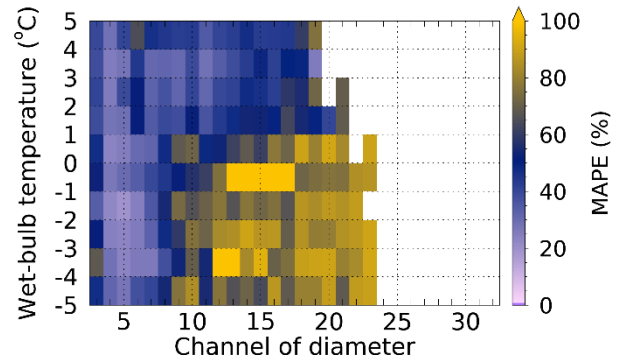
(c) Method 2



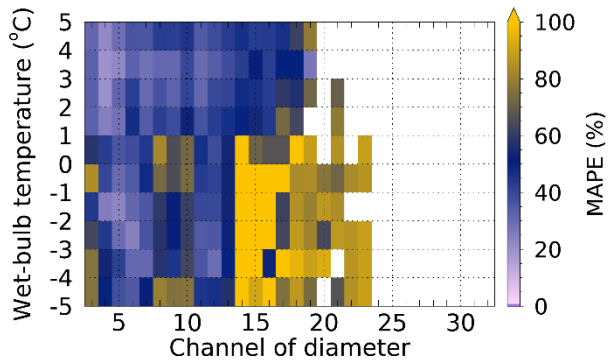
(d) Method 2 (melted)



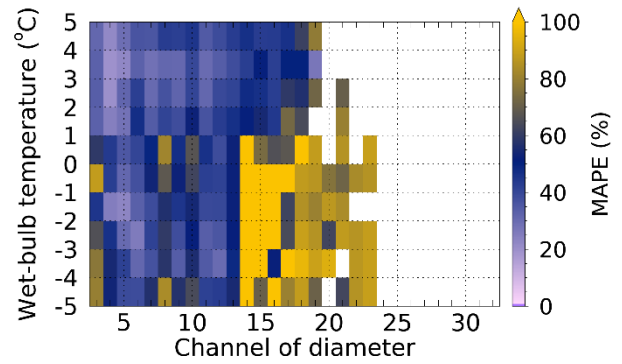
(e) Method 3



(f) Method 3 (melted)

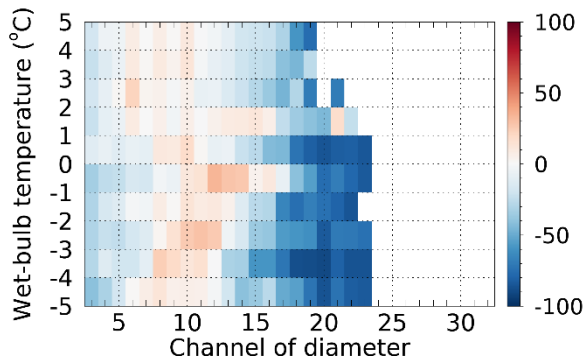


(a) Method 1

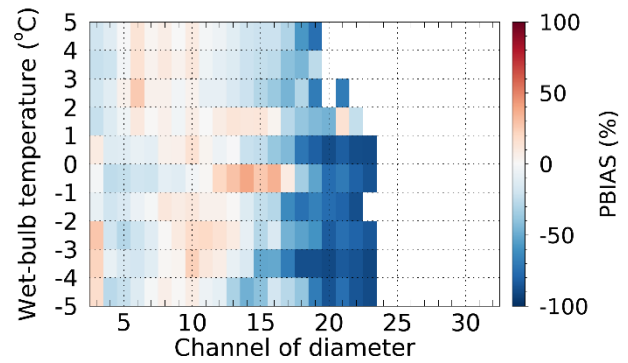


(b) Method 1 (melted)

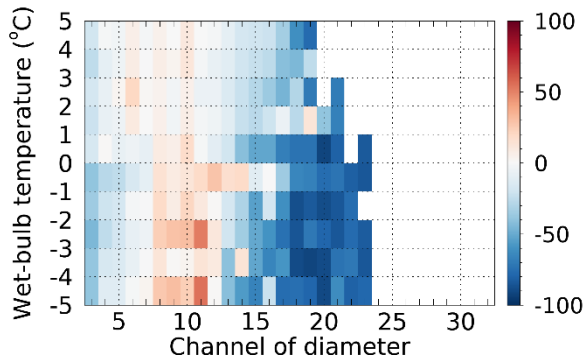
436 **Figure 16: MAPE for diameter and wet-bulb temperature using the pre-processing method**



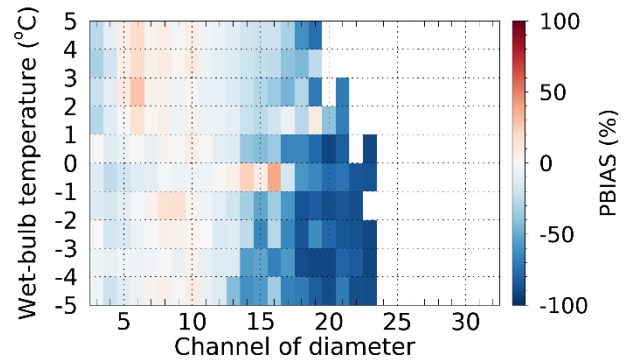
(c) Method 2



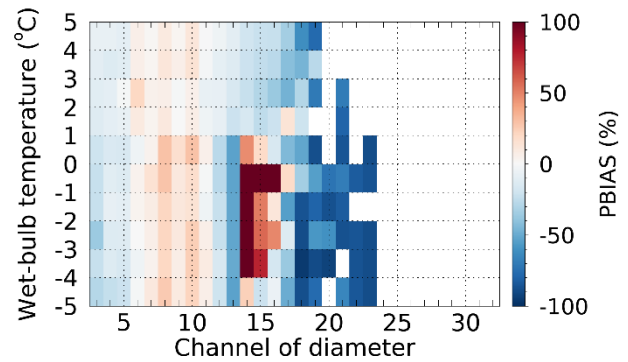
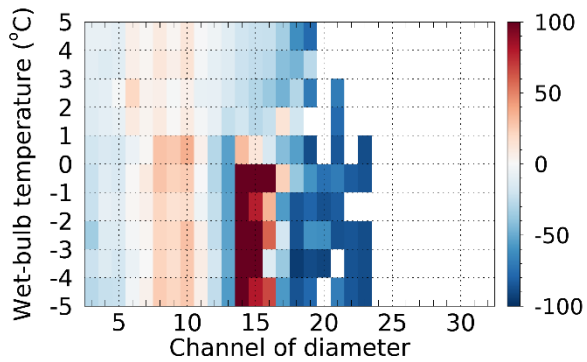
(d) Method 2 (melted)



(e) Method 3



(f) Method 3 (melted)



437 **Figure 17: PBAIS for diameter and wet-bulb temperature using the pre-processing method**

438 **5 Conclusion**

439 This study employed data collected from a 2DVD disdrometer in conjunction with traditional rain gauges to assess the
 440 precipitation measurements derived from the disdrometer under T_w conditions and to evaluate the reliability of the DSD
 441 model.

442 The precipitation estimates derived from the QC methods employed in this study exhibited $CC \geq 0.98$ when juxtaposed with
443 precipitation measurements obtained from rain gauges in an environment with T_w of 5 °C higher. The MAPE was
444 approximately 8.5%. In contrast to scenarios in which the QC method was not implemented, the propensity for the 2DVD
445 data to be overestimated diminished, and the overall error rate reduced. These findings indicate that all QC methods
446 demonstrated high reliability under rainfall conditions.

447 When T_{air} and T_w dropped below 1 °C, there was a notable reduction in the fall velocity of precipitation particles, which
448 became concentrated within a velocity range of approximately 0.5 to 3 m s⁻¹. Moreover, the ratio of snow particles to
449 raindrops considerably increased at temperatures below 1 °C for T_{air} and T_w . This observation is consistent with the findings
450 of Ding et al. (2014), which indicated that the proportion of rain was less than 30% at temperatures below this threshold.
451 Conversely, when T_{air} ranged from 1 to 3 °C, the distribution of fall velocities exhibited a broader range compared to
452 conditions where T_w was between 1 and 3 °C, resulting in a greater disparity with the terminal velocity of raindrops.
453 Consequently, it is justifiable to use T_w as a reference parameter to differentiate between types of precipitation using
454 disdrometer data.

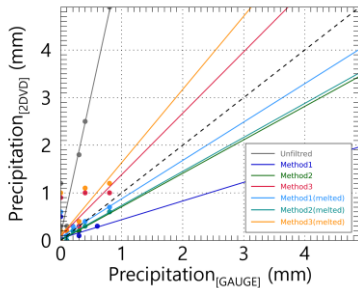
455 The fall velocity of particles exceeding 2 mm in diameter decreased within the 1 to 2 °C temperature range for T_w .
456 Conversely, at T_w below 1 °C, the observed results were outside the effective fall velocity range typically associated with
457 raindrops. Furthermore, as T_w decreased below 2 °C, the quantitative error, as measured by the correlation of disdrometer-
458 based precipitation data, increased. These results can be attributed to the fact that the filter ratio for particles measuring 3
459 mm or less escalated to 30% or higher when T_w was below 2 °C. Within this T_w range, it is plausible to regard raindrops and
460 solid particles as intermixed; consequently, implementing QC methods appropriate for conventional rainfall scenarios may
461 lead to inaccuracies. However, when snow particles were assumed to have undergone melting, the correlation approached
462 0.9, even within the temperature range of 0 to 1 °C, and the variability of the error decreased. These findings indicate that the
463 reliability of precipitation calculations can be maintained, even in scenarios where raindrops and snow particles coexist at
464 temperatures between 0 and 2 °C, provided that an appropriate density for snow particles is used. Additionally, it is
465 recommended that a weighing rain gauge be employed to verify precipitation when T_w is below 2 °C.

466 At 2 °C or higher T_w , the DSD shape remained consistent across different QC methods. However, as the temperature dropped
467 below 2 °C, Method 1, which defines the raindrop size interval as $\pm 40\%$ of the terminal velocity, indicated a comparatively
468 elevated number of drops measuring 2 mm or larger. In conditions where the temperature was below 1 °C, the application of
469 Method 3 (Raupach et al., 2015) resulted in a notable and irregular distribution of number concentration for droplet
470 diameters ranging from 1 to 2 mm. These findings can be attributed to the QC method employed, which raises concerns
471 about the reliability of the DSD parameters derived from the altered shape of the DSD. Consequently, it is imperative to use
472 disdrometer data corresponding to environmental conditions with temperatures of 2 °C or higher when calculating DSD
473 parameters and DSD-based rain rates.

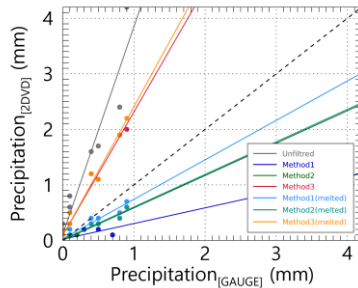
474 **Appendices**

475 Figures A1 and A2 present the findings from a comparative analysis of hourly accumulated precipitation intensity, derived
 476 from observations using the 2DVD and two types of rain gauges (A1 represents the tipping-bucket type and A2 represents
 477 the weighing type) under the specified T_w interval conditions at 1 °C intervals. In each figure, the solid line denotes the
 478 regression line correlating the precipitation intensities derived by applying each quality control (QC) method. The constants
 479 and validation indices associated with the regression lines are listed in Tables A1 and A2, respectively. Tables A3 and A4
 480 provide details regarding the diameter and velocity channels used to calculate the number concentration based on 2DVD data.
 481 The channel information corresponded to the values employed in the PARSIVEL disdrometer data.

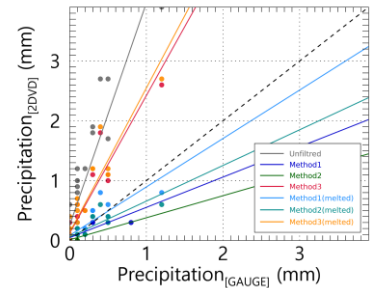
(a) $-5\text{ °C} \leq T_w < -4\text{ °C}$



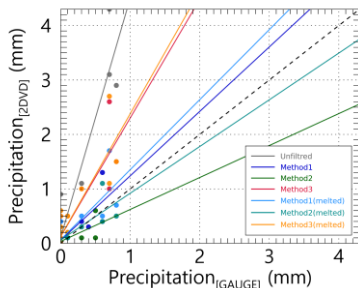
(b) $-4\text{ °C} \leq T_w < -3\text{ °C}$



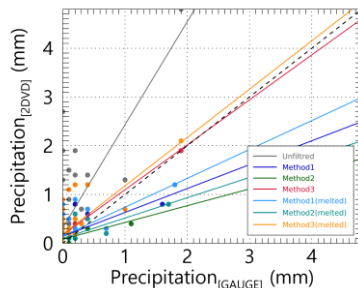
(c) $-3\text{ °C} \leq T_w < -2\text{ °C}$



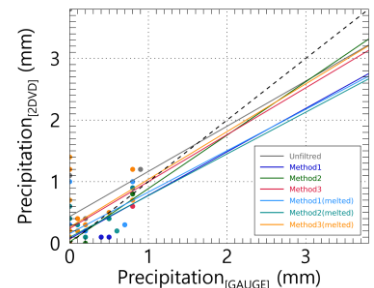
(d) $-2\text{ °C} \leq T_w < -1\text{ °C}$



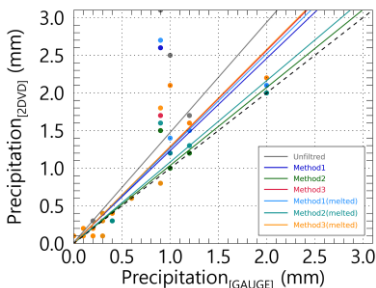
(e) $-1\text{ °C} \leq T_w < 0\text{ °C}$



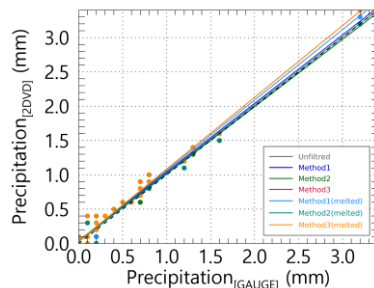
(f) $0\text{ °C} \leq T_w < 1\text{ °C}$



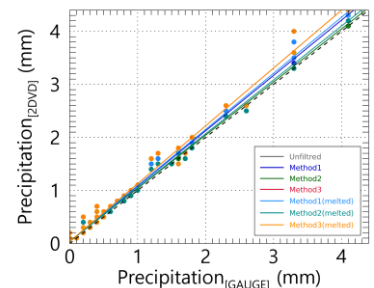
(g) $1\text{ °C} \leq T_w < 2\text{ °C}$



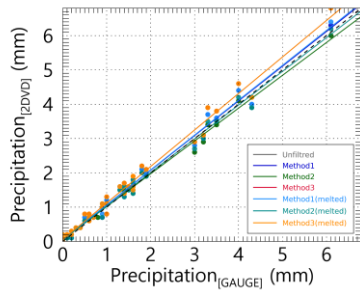
(h) $2\text{ °C} \leq T_w < 3\text{ °C}$



(i) $3\text{ °C} \leq T_w < 4\text{ °C}$

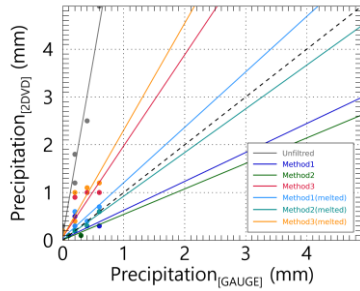


(j) $4\text{ °C} \leq T_w < 5\text{ °C}$

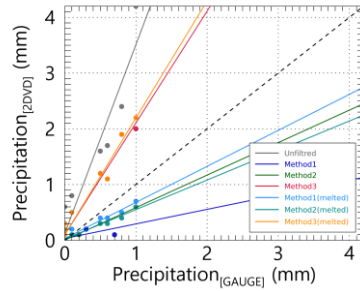


482 **Figure A1: Precipitation intensity scatter plot based on tipping-bucket rain gauge and 2DVD observation data for each T_w range.**
 483 **Each color in the scatter plot represents a filtering method.**

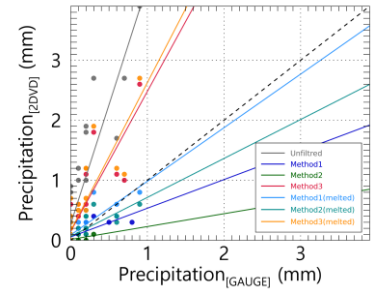
(a) $-5\text{ }^{\circ}\text{C} \leq T_w < -4\text{ }^{\circ}\text{C}$



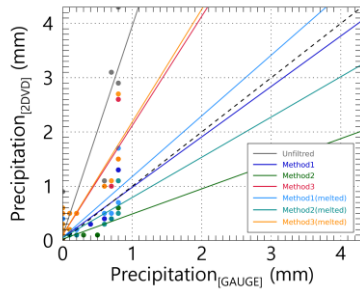
(b) $-4\text{ }^{\circ}\text{C} \leq T_w < -3\text{ }^{\circ}\text{C}$



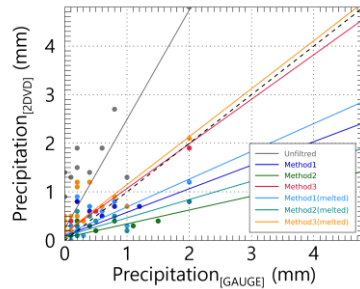
(c) $-3\text{ }^{\circ}\text{C} \leq T_w < -2\text{ }^{\circ}\text{C}$



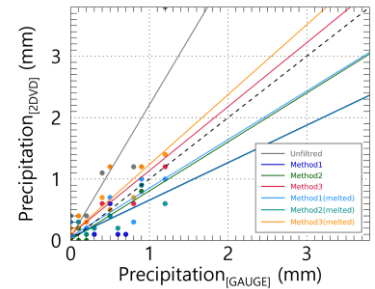
(d) $-2\text{ }^{\circ}\text{C} \leq T_w < -1\text{ }^{\circ}\text{C}$



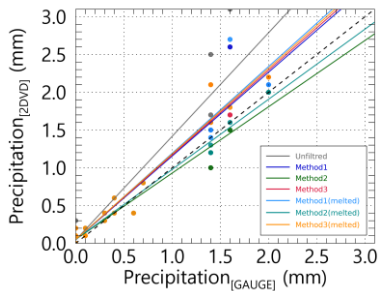
(e) $-1\text{ }^{\circ}\text{C} \leq T_w < 0\text{ }^{\circ}\text{C}$



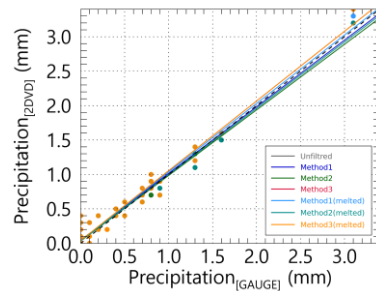
(f) $0\text{ }^{\circ}\text{C} \leq T_w < 1\text{ }^{\circ}\text{C}$



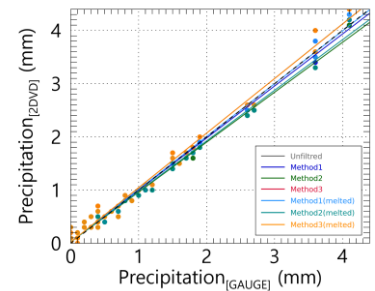
(g) $1\text{ }^{\circ}\text{C} \leq T_w < 2\text{ }^{\circ}\text{C}$



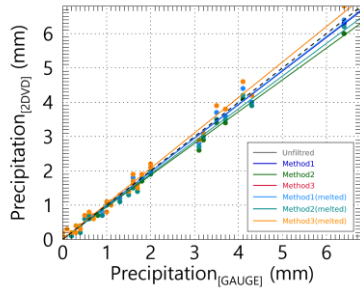
(h) $2\text{ }^{\circ}\text{C} \leq T_w < 3\text{ }^{\circ}\text{C}$



(i) $3\text{ }^{\circ}\text{C} \leq T_w < 4\text{ }^{\circ}\text{C}$



(j) $4\text{ }^{\circ}\text{C} \leq T_w < 5\text{ }^{\circ}\text{C}$



484 **Figure A2: Precipitation intensity scatter plot based on weighing rain gauge and 2DVD observation data for each T_w range. Each**
 485 **color in the scatter plot represents a filtering method.**

486 **Table A1: Comparison of precipitation intensity based on tipping-bucket rain gauge and 2DVD observation data for each T_w range.**

| | | T1 | T2 | T3 | T4 | T5 | T6 | T7 | T8 | T9 | T10 |
|------------|-------|-------|-------|-------|-------|-------|-------|-------|-------|-------|-------|
| Unfiltered | a_1 | 5.88 | 3.74 | 3.72 | 4.40 | 2.11 | 0.73 | 1.46 | 1.05 | 1.09 | 1.06 |
| | a_0 | 0.12 | 0.11 | 0.25 | 0.11 | 0.32 | 0.43 | 0.01 | 0.04 | 0.04 | 0.06 |
| | RMSE | 1.01 | 0.91 | 0.92 | 0.96 | 0.85 | 0.92 | 0.46 | 0.10 | 0.17 | 0.23 |
| | MAE | 0.44 | 0.47 | 0.56 | 0.45 | 0.45 | 0.40 | 0.16 | 0.06 | 0.10 | 0.16 |
| | MAPE | 48.71 | 55.32 | 60.15 | 50.58 | 50.86 | 43.25 | 34.45 | 15.68 | 13.54 | 21.14 |
| | CC | 0.97 | 0.97 | 0.93 | 0.95 | 0.74 | 0.23 | 0.85 | 0.99 | 0.99 | 0.99 |
| Method 1 | a_1 | 0.39 | 0.28 | 0.51 | 1.18 | 0.49 | 0.71 | 1.23 | 1.00 | 1.04 | 1.01 |
| | a_0 | 0.04 | 0.02 | 0.05 | 0.06 | 0.14 | 0.07 | 0.01 | 0.04 | 0.04 | 0.05 |
| | RMSE | 0.17 | 0.18 | 0.12 | 0.21 | 0.29 | 0.20 | 0.30 | 0.09 | 0.12 | 0.16 |
| | MAE | 0.08 | 0.07 | 0.05 | 0.11 | 0.15 | 0.11 | 0.10 | 0.06 | 0.07 | 0.12 |
| | MAPE | 28.57 | 56.67 | 27.24 | 34.01 | 37.07 | 56.39 | 31.27 | 17.96 | 12.04 | 16.83 |
| | CC | 0.45 | 0.75 | 0.78 | 0.79 | 0.55 | 0.66 | 0.89 | 0.99 | 1.00 | 0.99 |
| Method 2 | a_1 | 0.70 | 0.58 | 0.37 | 0.59 | 0.34 | 0.87 | 1.03 | 0.98 | 1.00 | 0.96 |
| | a_0 | 0.01 | 0.00 | 0.01 | 0.03 | 0.08 | 0.02 | 0.00 | 0.03 | 0.04 | 0.06 |
| | RMSE | 0.03 | 0.03 | 0.06 | 0.13 | 0.20 | 0.09 | 0.12 | 0.08 | 0.08 | 0.13 |
| | MAE | 0.01 | 0.01 | 0.04 | 0.07 | 0.10 | 0.06 | 0.05 | 0.05 | 0.05 | 0.09 |
| | MAPE | 5.56 | 11.11 | 23.81 | 57.78 | 41.67 | 26.56 | 26.79 | 12.78 | 10.54 | 13.44 |
| | CC | 0.98 | 0.94 | 0.60 | 0.67 | 0.57 | 0.91 | 0.97 | 0.99 | 1.00 | 1.00 |
| Method 3 | a_1 | 1.29 | 2.22 | 2.30 | 2.18 | 0.92 | 0.76 | 1.28 | 1.05 | 1.09 | 1.06 |
| | a_0 | 0.09 | 0.09 | 0.12 | 0.13 | 0.18 | 0.24 | 0.00 | 0.04 | 0.04 | 0.06 |
| | RMSE | 0.24 | 0.44 | 0.47 | 0.49 | 0.33 | 0.43 | 0.25 | 0.10 | 0.17 | 0.23 |
| | MAE | 0.11 | 0.26 | 0.28 | 0.26 | 0.18 | 0.23 | 0.10 | 0.06 | 0.10 | 0.16 |
| | MAPE | 38.75 | 49.04 | 51.11 | 47.07 | 45.58 | 46.25 | 25.58 | 15.68 | 13.54 | 21.14 |

| | | | | | | | | | | | |
|----------------------|-------|-------|-------|-------|-------|-------|-------|-------|-------|-------|-------|
| | CC | 0.76 | 0.99 | 0.94 | 0.87 | 0.73 | 0.47 | 0.94 | 0.99 | 0.99 | 0.99 |
| Method 1 (melted) | a_1 | 0.81 | 0.71 | 0.81 | 1.29 | 0.59 | 0.67 | 1.26 | 1.03 | 1.06 | 1.02 |
| | a_0 | 0.07 | 0.03 | 0.08 | 0.07 | 0.15 | 0.16 | 0.01 | 0.04 | 0.03 | 0.05 |
| | RMSE | 0.16 | 0.10 | 0.15 | 0.25 | 0.28 | 0.31 | 0.32 | 0.09 | 0.13 | 0.16 |
| | MAE | 0.06 | 0.05 | 0.09 | 0.12 | 0.16 | 0.16 | 0.11 | 0.06 | 0.08 | 0.12 |
| | MAPE | 26.33 | 21.39 | 34.06 | 31.87 | 42.73 | 38.50 | 31.64 | 18.03 | 12.37 | 16.51 |
| | CC | 0.76 | 0.97 | 0.85 | 0.82 | 0.66 | 0.51 | 0.88 | 0.99 | 1.00 | 0.99 |
| Method 2 (melted) | a_1 | 0.71 | 0.59 | 0.60 | 0.86 | 0.42 | 0.68 | 1.08 | 0.99 | 1.02 | 0.98 |
| | a_0 | 0.02 | 0.02 | 0.06 | 0.06 | 0.10 | 0.10 | 0.00 | 0.03 | 0.04 | 0.05 |
| | RMSE | 0.09 | 0.14 | 0.15 | 0.17 | 0.25 | 0.21 | 0.14 | 0.08 | 0.09 | 0.13 |
| | MAE | 0.05 | 0.07 | 0.08 | 0.09 | 0.13 | 0.12 | 0.06 | 0.05 | 0.05 | 0.10 |
| | MAPE | 17.78 | 23.33 | 27.88 | 31.87 | 45.37 | 44.88 | 27.62 | 12.84 | 11.00 | 15.80 |
| | CC | 0.93 | 0.98 | 0.84 | 0.79 | 0.67 | 0.65 | 0.96 | 0.99 | 1.00 | 1.00 |
| Method 3 (melted) | a_1 | 1.54 | 2.33 | 2.41 | 2.25 | 0.99 | 0.77 | 1.29 | 1.05 | 1.09 | 1.06 |
| | a_0 | 0.10 | 0.08 | 0.14 | 0.13 | 0.19 | 0.26 | 0.00 | 0.04 | 0.04 | 0.06 |
| | RMSE | 0.27 | 0.46 | 0.51 | 0.51 | 0.35 | 0.46 | 0.26 | 0.10 | 0.17 | 0.23 |
| | MAE | 0.13 | 0.27 | 0.30 | 0.28 | 0.20 | 0.25 | 0.11 | 0.06 | 0.10 | 0.16 |
| | MAPE | 40.50 | 49.24 | 50.27 | 47.38 | 46.46 | 45.30 | 28.44 | 15.68 | 13.54 | 21.14 |
| | CC | 0.79 | 0.99 | 0.93 | 0.87 | 0.74 | 0.45 | 0.93 | 0.99 | 0.99 | 0.99 |

487

488 **Table A2: Comparison of precipitation intensity based on weighing rain gauge and 2DVD observation data for each T_w range.**

| | | T1 | T2 | T3 | T4 | T5 | T6 | T7 | T8 | T9 | T10 |
|------------|-------|-------|-------|-------|-------|-------|-------|-------|-------|-------|-------|
| Unfiltered | a_1 | 7.36 | 3.39 | 3.98 | 3.86 | 2.25 | 2.15 | 1.37 | 1.01 | 1.03 | 1.03 |
| | a_0 | 0.09 | 0.12 | 0.27 | 0.09 | 0.24 | 0.06 | 0.04 | 0.04 | 0.02 | 0.01 |
| | RMSE | 1.04 | 0.88 | 0.95 | 0.93 | 0.76 | 0.64 | 0.33 | 0.14 | 0.12 | 0.17 |
| | MAE | 0.44 | 0.46 | 0.57 | 0.43 | 0.43 | 0.31 | 0.15 | 0.08 | 0.07 | 0.12 |
| | MAPE | 49.76 | 55.42 | 60.80 | 48.81 | 53.44 | 41.61 | 41.39 | 22.03 | 13.07 | 19.05 |
| | CC | 0.98 | 0.97 | 0.90 | 0.93 | 0.88 | 0.89 | 0.95 | 0.98 | 0.99 | 0.99 |
| Method 1 | a_1 | 0.61 | 0.26 | 0.48 | 0.93 | 0.48 | 0.61 | 1.11 | 0.97 | 0.98 | 0.98 |
| | a_0 | 0.02 | 0.03 | 0.06 | 0.05 | 0.09 | 0.05 | 0.04 | 0.05 | 0.02 | 0.01 |
| | RMSE | 0.13 | 0.17 | 0.13 | 0.19 | 0.28 | 0.20 | 0.20 | 0.13 | 0.10 | 0.14 |
| | MAE | 0.06 | 0.07 | 0.07 | 0.12 | 0.13 | 0.11 | 0.10 | 0.08 | 0.07 | 0.10 |
| | MAPE | 25.71 | 63.33 | 41.35 | 41.49 | 36.12 | 79.17 | 38.21 | 22.17 | 14.21 | 21.89 |
| | CC | 0.70 | 0.65 | 0.73 | 0.80 | 0.79 | 0.71 | 0.96 | 0.98 | 0.99 | 1.00 |

| | | | | | | | | | | | |
|----------------------|-------|-------|-------|-------|-------|-------|-------|-------|-------|-------|-------|
| Method 2 | a_1 | 0.53 | 0.58 | 0.21 | 0.46 | 0.28 | 0.80 | 0.88 | 0.95 | 0.94 | 0.93 |
| | a_0 | 0.01 | 0.00 | 0.01 | 0.03 | 0.06 | 0.01 | 0.05 | 0.03 | 0.03 | 0.02 |
| | RMSE | 0.07 | 0.03 | 0.09 | 0.18 | 0.31 | 0.10 | 0.11 | 0.12 | 0.11 | 0.17 |
| | MAE | 0.02 | 0.01 | 0.06 | 0.11 | 0.15 | 0.07 | 0.07 | 0.07 | 0.07 | 0.12 |
| | MAPE | 22.22 | 11.11 | 28.57 | 85.56 | 55.43 | 27.34 | 35.56 | 18.32 | 14.12 | 20.69 |
| | CC | 0.82 | 0.94 | 0.45 | 0.75 | 0.78 | 0.92 | 0.98 | 0.98 | 1.00 | 1.00 |
| Method 3 | a_1 | 1.91 | 2.01 | 2.33 | 2.02 | 0.92 | 1.04 | 1.12 | 1.01 | 1.03 | 1.03 |
| | a_0 | 0.07 | 0.10 | 0.15 | 0.10 | 0.15 | 0.10 | 0.05 | 0.04 | 0.02 | 0.01 |
| | RMSE | 0.22 | 0.41 | 0.52 | 0.45 | 0.29 | 0.21 | 0.16 | 0.14 | 0.12 | 0.17 |
| | MAE | 0.12 | 0.25 | 0.29 | 0.24 | 0.16 | 0.13 | 0.09 | 0.08 | 0.07 | 0.12 |
| | MAPE | 42.13 | 49.58 | 52.32 | 44.83 | 46.50 | 37.92 | 34.21 | 22.03 | 13.07 | 19.05 |
| | CC | 0.91 | 0.98 | 0.86 | 0.90 | 0.80 | 0.90 | 0.98 | 0.98 | 0.99 | 0.99 |
| Method 1 (melted) | a_1 | 1.16 | 0.65 | 0.89 | 1.12 | 0.57 | 0.79 | 1.15 | 0.99 | 0.99 | 0.98 |
| | a_0 | 0.05 | 0.03 | 0.09 | 0.06 | 0.12 | 0.06 | 0.04 | 0.04 | 0.02 | 0.01 |
| | RMSE | 0.11 | 0.13 | 0.16 | 0.23 | 0.26 | 0.16 | 0.21 | 0.13 | 0.10 | 0.13 |
| | MAE | 0.06 | 0.08 | 0.10 | 0.11 | 0.15 | 0.10 | 0.09 | 0.08 | 0.06 | 0.10 |
| | MAPE | 30.25 | 31.05 | 36.50 | 29.44 | 49.92 | 32.10 | 37.80 | 22.22 | 13.91 | 21.50 |
| | CC | 0.90 | 0.97 | 0.82 | 0.82 | 0.77 | 0.89 | 0.96 | 0.98 | 1.00 | 1.00 |
| Method 2 (melted) | a_1 | 0.91 | 0.53 | 0.65 | 0.74 | 0.38 | 0.61 | 0.93 | 0.96 | 0.95 | 0.95 |
| | a_0 | 0.01 | 0.02 | 0.07 | 0.05 | 0.09 | 0.04 | 0.05 | 0.04 | 0.02 | 0.01 |
| | RMSE | 0.04 | 0.18 | 0.14 | 0.17 | 0.29 | 0.18 | 0.09 | 0.12 | 0.11 | 0.15 |
| | MAE | 0.01 | 0.10 | 0.09 | 0.11 | 0.14 | 0.10 | 0.06 | 0.07 | 0.07 | 0.11 |
| | MAPE | 8.89 | 35.56 | 34.62 | 42.75 | 58.79 | 40.35 | 34.42 | 17.78 | 14.24 | 22.16 |
| | CC | 0.98 | 0.98 | 0.79 | 0.82 | 0.77 | 0.87 | 0.99 | 0.98 | 1.00 | 1.00 |
| Method 3 (melted) | a_1 | 2.24 | 2.10 | 2.47 | 2.08 | 0.99 | 1.14 | 1.13 | 1.01 | 1.03 | 1.03 |
| | a_0 | 0.07 | 0.10 | 0.16 | 0.11 | 0.16 | 0.10 | 0.05 | 0.04 | 0.02 | 0.01 |
| | RMSE | 0.27 | 0.44 | 0.55 | 0.48 | 0.30 | 0.22 | 0.16 | 0.14 | 0.12 | 0.17 |
| | MAE | 0.14 | 0.26 | 0.32 | 0.25 | 0.17 | 0.14 | 0.09 | 0.08 | 0.07 | 0.12 |
| | MAPE | 43.48 | 49.81 | 51.47 | 45.14 | 46.83 | 38.15 | 37.14 | 22.03 | 13.07 | 19.05 |
| | CC | 0.93 | 0.98 | 0.86 | 0.89 | 0.82 | 0.92 | 0.98 | 0.98 | 0.99 | 0.99 |

489 **Table A3: Diameter channel information of the PARSIVEL disdrometer.**

| Channel number | Mid-value of channel (mm) | Diameter spread (mm) | Channel number | Mid-value of channel (mm) | Diameter spread (mm) |
|----------------|---------------------------|----------------------|----------------|---------------------------|----------------------|
| 1 | 0.062 | 0.125 | 17 | 3.250 | 0.500 |

| | | | | | | |
|----|-------|-------|--|----|--------|-------|
| 2 | 0.187 | 0.125 | | 18 | 3.750 | 0.500 |
| 3 | 0.312 | 0.125 | | 19 | 4.250 | 0.500 |
| 4 | 0.437 | 0.125 | | 20 | 4.750 | 0.500 |
| 5 | 0.562 | 0.125 | | 21 | 5.500 | 1.000 |
| 6 | 0.687 | 0.125 | | 22 | 6.500 | 1.000 |
| 7 | 0.812 | 0.125 | | 23 | 7.500 | 1.000 |
| 8 | 0.937 | 0.125 | | 24 | 8.500 | 1.000 |
| 9 | 1.062 | 0.125 | | 25 | 9.500 | 1.000 |
| 10 | 1.187 | 0.125 | | 26 | 11.000 | 2.000 |
| 11 | 1.375 | 0.250 | | 27 | 13.000 | 2.000 |
| 12 | 1.625 | 0.250 | | 28 | 15.000 | 2.000 |
| 13 | 1.875 | 0.250 | | 29 | 17.000 | 2.000 |
| 14 | 2.125 | 0.250 | | 30 | 19.000 | 2.000 |
| 15 | 2.375 | 0.250 | | 31 | 21.500 | 3.000 |
| 16 | 2.750 | 0.500 | | 32 | 24.500 | 3.000 |

490 **Table A4: Velocity channel information of the PARSIVEL disdrometer.**

| Channel number | Mid-value of channel (mm) | Velocity spread (mm) | | Channel number | Mid-value of channel (mm) | Velocity spread (mm) |
|----------------|---------------------------|----------------------|--|----------------|---------------------------|----------------------|
| 1 | 0.050 | 0.100 | | 17 | 2.600 | 0.400 |
| 2 | 0.150 | 0.100 | | 18 | 3.000 | 0.400 |
| 3 | 0.250 | 0.100 | | 19 | 3.400 | 0.400 |
| 4 | 0.350 | 0.100 | | 20 | 3.800 | 0.400 |
| 5 | 0.450 | 0.100 | | 21 | 4.400 | 0.800 |
| 6 | 0.550 | 0.100 | | 22 | 5.200 | 0.800 |
| 7 | 0.650 | 0.100 | | 23 | 6.000 | 0.800 |
| 8 | 0.750 | 0.100 | | 24 | 6.800 | 0.800 |
| 9 | 0.850 | 0.100 | | 25 | 7.600 | 0.800 |
| 10 | 0.950 | 0.100 | | 26 | 8.800 | 1.600 |
| 11 | 1.100 | 0.200 | | 27 | 10.400 | 1.600 |
| 12 | 1.300 | 0.200 | | 28 | 12.000 | 1.600 |
| 13 | 1.500 | 0.200 | | 29 | 13.600 | 1.600 |
| 14 | 1.700 | 0.200 | | 30 | 15.200 | 1.600 |

| | | | | | | |
|----|-------|-------|--|----|--------|-------|
| 15 | 1.900 | 0.200 | | 31 | 17.600 | 3.200 |
| 16 | 2.200 | 0.400 | | 32 | 20.800 | 3.200 |

491 **Author contributions**

492 HJK and CJ, conceptualized the project. JB did the data curation and formal analysis. HJK and SHS did the analysis and
493 interpretation. HJK and JB led the investigation. HJK prepared the original draft, and SHS and CJ reviewed and edited the
494 paper. All authors have read and agreed to the published version of the paper.

495 **Acknowledgements**

496 This study was supported by the Basic Science Research Program through the National Research Foundation of Korea
497 (NRF), funded by the Ministry of Education (RS-2022-NR071182).

498

499 **Competing Interest**

500 The contact author has declared that none of the authors has any competing interests.

501 **References**

- 502 Atlas, D., Srivastava, R. C., and Sekhon, R. S.: Doppler radar characteristics of precipitation at vertical incidence, *Rev.*
503 *Geophys.*, 11, 1–35. <https://doi.org/10.1029/RG011i001p00001>, 1973.
- 504 Barthazy, E. and Schefold, R.: Fall velocity of snowflakes of different riming degree and crystal types, *Atmos. Res.*, 82,
505 391–398. <https://doi.org/10.1016/j.atmosres.2005.12.009>, 2006.
- 506 Beard, K. V.: Terminal velocity adjustment for cloud and precipitation drops aloft, *J. Atmos. Sci.*, 34, 1293–1298.
507 [https://doi.org/10.1175/1520-0469\(1977\)034<1293:TVAFCA>2.0.CO;2](https://doi.org/10.1175/1520-0469(1977)034<1293:TVAFCA>2.0.CO;2), 1977.
- 508 Brandes, E. A., Zhang, G., and Vivekanandan, J.: Experiments in rainfall estimation with a polarimetric radar in a
509 subtropical environment, *J. Appl. Meteor.*, 41, 674–685. [https://doi.org/10.1175/1520-0450\(2002\)041<0674:EIREWA>2.0.CO;2](https://doi.org/10.1175/1520-0450(2002)041<0674:EIREWA>2.0.CO;2), 2002.
- 511 Chang, W. Y., Wang, T. C. C., and Lin, P. L.: Characteristics of the raindrop size distribution and drop shape relation in
512 typhoon systems in the western Pacific from the 2D video disdrometer and NCU C-band polarimetric radar, *J. Atmos.*
513 *Ocean. Technol.*, 26, 1973–1993. <https://doi.org/10.1175/2009JTECHA1236.1>, 2009.
- 514 Dahlström, B.: Cloud physical and climatological factors for the determination of rain intensity, *Water*, 13, 2292.
515 <https://doi.org/10.3390/w13162292>, 2021.
- 516 Delanoë, J., Protat, A., Testud, J., Bouniol, D., Heymsfield, A. J., Bansemmer, A., Brown, P. R. A., Forbes, R. M.: Statistical
517 properties of the normalized ice particle size distribution, *J. Geophys. Res. Atmos.*, 110.
518 <https://doi.org/10.1029/2004JD005405>, 2005.

519 Deo, A. and Walsh, K. J. E.: Contrasting tropical cyclone and non-tropical cyclone related rainfall drop size distribution at
520 Darwin, Australia, *Atmos. Res.*, 181, 81–94. <https://doi.org/10.1016/j.atmosres.2016.06.015>, 2016.

521 Ding, B., Yang, K., Qin, J., Wang, L., Chen, Y., and He, X.: The dependence of precipitation types on surface elevation and
522 meteorological conditions and its parameterization, *J. Hydrol.*, 513, 154–163.
523 <https://doi.org/10.1016/j.jhydrol.2014.03.038>, 2014.

524 Du, Y. and Chen, G.: Heavy rainfall associated with double low-level jets over southern China. Part II: Convection initiation,
525 *Mon. Weather Rev.*, 147, 543–565. <https://doi.org/10.1175/MWR-D-18-0102.1>, 2019.

526 Friedrich, K., Kalina, E. A., Masters, F. J., and Lopez, C. R.: Drop-size distributions in thunderstorms measured by optical
527 disdrometers during VORTEX2, *Mon. Weather Rev.*, 141, 1182–1203. <https://doi.org/10.1175/MWR-D-12-00116.1>,
528 2013.

529 Gong, Y., He, T., Chen, M., Wang, B., Nie, L., and Yin, Y.: Spatio-temporal enhanced contrastive and contextual learning
530 for weather forecasting, *IEEE Trans. Knowl. Data Eng.*, 36, 4260–4274. <https://doi.org/10.1109/TKDE.2024.3362825>,
531 2024.

532 Grazioli, J., Tuia, D., Monhart, S., Schneebeli, M., Raupach, T., and Berne, A.: Hydrometeor classification from two-
533 dimensional video disdrometer data, *Atmos. Meas. Tech.*, 7, 2869–2882. <https://doi.org/10.5194/amt-7-2869-2014>,
534 2014.

535 Guo, J., Liu, H., Li, Z., Rosenfeld, D., Jiang, M., Xu, W., Jiang, J. H., He, J., Chen, D., Min, M., Zhai, P.: Aerosol-induced
536 changes in the vertical structure of precipitation: A perspective of TRMM precipitation radar, *Atmos. Chem. Phys.*, 18,
537 13329–13343. <https://doi.org/10.5194/acp-18-13329-2018>, 2018.

538 Hu, A. Z. and Igel, A. L.: A bin and a bulk microphysics scheme can be more alike than two bin schemes, *J. Adv. Model.*
539 *Earth Syst.*, 15, MS003303, e2022. <https://doi.org/10.1029/2022MS003303>, 2023.

540 Insel, N., Poulsen, C. J., and Ehlers, T. A.: Influence of the Andes Mountains on South American moisture transport,
541 convection, and precipitation, *Clim. Dyn.*, 35, 1477–1492. <https://doi.org/10.1007/s00382-009-0637-1>, 2010.

542 Iversen, E. C., Thompson, G., and Nygaard, B. E.: Improvements to melting snow behavior in a bulk microphysics scheme,
543 *Atmos. Res.*, 253, 105471. <https://doi.org/10.1016/j.atmosres.2021.105471>, 2021.

544 Jaffrain, J. and Berne, A.: Experimental quantification of the sampling uncertainty associated with measurements from
545 PARSIVEL disdrometers, *J. Hydrol. Meteorol.*, 12, 352–370. <https://doi.org/10.1175/2010JHM1244.1>, 2011.

546 Ji, L., Chen, H., Li, L., Chen, B., Xiao, X., Chen, M., and Zhang, G.: Raindrop size distributions and rain characteristics
547 observed by a PARSIVEL disdrometer in Beijing, Northern China, *Remote Sens.*, 11, 1479.
548 <https://doi.org/10.3390/rs11121479>, 2019.

549 Kim, H. J., Jung, W., Suh, S. H., Lee, D. I., and You, C. H.: The characteristics of raindrop size distribution at windward and
550 leeward side over mountain area, *Remote Sens.*, 14, 2419. <https://doi.org/10.3390/rs14102419>, 2022.

551 Kim, H. J., Lee, K. O., You, C. H., Uyeda, H., and Lee, D. I.: Microphysical characteristics of a convective precipitation
552 system observed on July 04, 2012, over Mt. Halla in South Korea, *Atmos. Res.*, 222, 74–87.
553 <https://doi.org/10.1016/j.atmosres.2019.02.011>, 2019.

554 Kochendorfer, J., Earle, M. E., Hodyss, D., Reverdin, A., Roulet, Y. A., Nitu, R., Rasmussen, R., Landolt, S., Buisán, S.,
555 Laine, T.: Undercatch adjustments for tipping-bucket gauge measurements of solid precipitation, *J. Hydrol. Meteorol.*,
556 21, 1193–1205. <https://doi.org/10.1175/JHM-D-19-0256.1>, 2020.

557 Kruger, A. and Krajewski, W. F.: Two-dimensional video disdrometer: A description, *J. Atmos. Ocean. Technol.*, 19, 602–
558 617. [https://doi.org/10.1175/1520-0426\(2002\)019<0602:TDVDAD>2.0.CO;2](https://doi.org/10.1175/1520-0426(2002)019<0602:TDVDAD>2.0.CO;2), 2002.

559 Lee, K. O., Uyeda, H., and Lee, D. I.: Microphysical structures associated with enhancement of convective cells over Mt.
560 Halla, Jeju Island, Korea on 6 July 2007, *Atmos. Res.*, 135–136, 76–90.
561 <https://doi.org/10.1016/j.atmosres.2013.08.012>, 2014.

562 Lintner, B. R., Adams, D. K., Schiro, K. A., Stansfield, A. M., Amorim Rocha, A. A., and Neelin, J. D.: Relationships
563 among climatological vertical moisture structure, column water vapor, and precipitation over the central Amazon in
564 observations and CMIP5 models, *Geophys. Res. Lett.*, 44, 1981–1989. <https://doi.org/10.1002/2016GL071923>, 2017.

565 Liu, X., Li, H., Hu, S., Wan, Q., Xiao, H., Zheng, T., Li, M., Ye, L., Guo, Z., Wang, Y., Yan, Z.: A high-precision and fast
566 solution method of gamma raindrop size distribution based on 0-moment and 3-moment in South China, *J. Appl.*
567 *Meteorol. Climatol.*, 60, 1407–1421. <https://doi.org/10.1175/JAMC-D-21-0043.1>, 2021.

568 Lu, Y., Yu, Z., Albertson, J. D., Chen, H., Hu, L., Pendergrass, A., Chen, X., Li, Q.: Understanding the influence of urban
569 form on the spatial pattern of precipitation, *Earths Future*, 12, EF003846, e2023.
570 <https://doi.org/10.1029/2023EF003846>, 2024.

571 Maheskumar, R. S., Padmakumari, B., Konwar, M., Morwal, S. B., and Deshpande, C. G.: Characterization of hydrometeors
572 and precipitation over the Indian monsoon region using aircraft measurements, *Atmos. Res.*, 205, 147–154.
573 <https://doi.org/10.1016/j.atmosres.2018.02.012>, 2018.

574 Marshall, J. S. and Palmer, W. M. K.: The distribution of raindrops with size, *J. Atmos. Sci.*, 5, 165–166.
575 [https://doi.org/10.1175/1520-0469\(1948\)005,0165:TDORWS.2.0.CO;2](https://doi.org/10.1175/1520-0469(1948)005,0165:TDORWS.2.0.CO;2), 1948.

576 Marzuki, M., Randeu, W. L., Schönhuber, M., Bringi, V. N., Kozu, T., and Shimomai, T.: Raindrop size distribution
577 parameters of distrometer data with different bin sizes, *IEEE Trans. Geosci. Remote Sens.*, 48, 3075–3080.
578 <https://doi.org/10.1109/TGRS.2010.2043955>, 2010.

579 Ong, C. R., Miura, H., Koike, M.: The terminal velocity of axisymmetric cloud drops and raindrops evaluated by the
580 immersed boundary method. *J. Atmos. Sci.*, 78(4), 1129–1146. <https://doi.org/10.1175/JAS-D-20-0161.1>, 2021.

581 Padullés, R., Kuo, Y. H., Neelin, J. D., Turk, F. J., Ao, C. O., and De la Torre Juárez, M.: Global tropical precipitation
582 relationships to free-tropospheric water vapor using radio occultations, *J. Atmos. Sci.*, 79, 1585–1600.
583 <https://doi.org/10.1175/JAS-D-21-0052.1>, 2022.

584 Raupach, T. H. and Berne, A.: Correction of raindrop size distributions measured by Parsivel disdrometers, using a two-
585 dimensional video disdrometer as a reference, *Atmos. Meas. Tech.*, 8, 343–365. [https://doi.org/10.5194/amt-8-343-](https://doi.org/10.5194/amt-8-343-2015)
586 [2015](https://doi.org/10.5194/amt-8-343-2015), 2015.

587 Savina, M., Schätti, B., Molnar, P., Burlando, P., and Sevruck, B.: Comparison of a tipping-bucket and electronic weighing
588 precipitation gage for snowfall, *Atmos. Res.*, 103, 45–51. <https://doi.org/10.1016/j.atmosres.2011.06.010>, 2012.

589 Segovia-Cardozo, D. A., Rodríguez-Sinobas, L., Díez-Herrero, A., Zubelzu, S., and Canales-Ide, F.: Understanding the
590 mechanical biases of tipping-bucket rain gauges: A semi-analytical calibration approach, *Water*, 13, 2285.
591 <https://doi.org/10.3390/w13162285>, 2021.

592 Serio, M. A., Carollo, F. G., and Ferro, V.: Raindrop size distribution and terminal velocity for rainfall erosivity studies. A
593 review, *J. Hydrol.*, 576, 210–228. <https://doi.org/10.1016/j.jhydrol.2019.06.040>, 2019.

594 Smith, P. L.: Raindrop size distributions: Exponential or gamma—Does the difference matter?, *J. Appl. Meteor.*, 42, 1031–
595 1034. [https://doi.org/10.1175/1520-0450\(2003\)042<1031:RSDEOG>2.0.CO;2](https://doi.org/10.1175/1520-0450(2003)042<1031:RSDEOG>2.0.CO;2), 2003.

596 Steenburgh, W. J.: Sea-effect precipitation: A Look at Japan’s “Gosetsu Chitai”, *Bull. Am. Meteorol. Soc.*, 101, 129–136.
597 <https://doi.org/10.1175/BAMS-D-18-0335.A>, 2020.

598 Stull, R.: Wet-bulb temperature from relative humidity and air temperature, *J. Appl. Meteorol. Climatol.*, 50, 2267–2269.
599 <https://doi.org/10.1175/JAMC-D-11-0143.1>, 2011.

600 Sypka, P.: Dynamic real-time volumetric correction for tipping-bucket rain gauges, *Agric. Forest Meteorol.*, 271, 158–167.
601 <https://doi.org/10.1016/j.agrformet.2019.02.044>, 2019.

602 Tang, Y. S., Chang, P. L., Chang, W. Y., Zhang, J., Tang, L., Lin, P. F., and Chen, C. R.: A localized quantitative
603 precipitation estimation for S-band polarimetric radar in Taiwan, *J. Hydrol. Meteorol.*, 25, 1697–1712.
604 <https://doi.org/10.1175/JHM-D-23-0205.1>, 2024.

605 Thomas, A., Kanawade, V. P., Chakravarty, K., and Srivastava, A. K.: Characterization of raindrop size distributions and its
606 response to cloud microphysical properties, *Atmos. Res.*, 249, 105292.
607 <https://doi.org/10.1016/j.atmosres.2020.105292>, 2021.

608 Thurai, M. and Bringi, V. N.: Drop axis ratios from a 2D video disdrometer, *J. Atmos. Ocean. Technol.*, 22, 966–978.
609 <https://doi.org/10.1175/JTECH1767.1>, 2005.

610 Tiira, J., Moisseev, D. N., Von Lerber, A., Ori, D., Tokay, A., Bliven, L. F., and Petersen, W.: Ensemble mean density and
611 its connection to other microphysical properties of falling snow as observed in Southern Finland, *Atmos. Meas. Tech.*,
612 9, 4825–4841. <https://doi.org/10.5194/amt-9-4825-2016>, 2016.

613 Ulbrich, C. W.: Natural variations in the analytical form of the raindrop size distribution, *J. Clim. Appl. Meteorol.*, 22, 1764–
614 1775. [https://doi.org/10.1175/1520-0450\(1983\)022<1764:NVITAF>2.0.CO;2](https://doi.org/10.1175/1520-0450(1983)022<1764:NVITAF>2.0.CO;2), 1983.

615 Vázquez-Martín, S., Kuhn, T., and Eliasson, S.: Mass of different snow crystal shapes derived from fall speed measurements,
616 *Atmos. Chem. Phys.*, 21, 18669–18688. <https://doi.org/10.5194/acp-21-18669-2021>, 2021.

617 Wang, P. K. and Pruppacher, H. R.: Acceleration to terminal velocity of cloud and raindrops. *J. Appl. Meteorol. Clim.*, 16(3),
618 275–280. [https://doi.org/10.1175/1520-0450\(1977\)016<0275:ATTVOC>2.0.CO;2](https://doi.org/10.1175/1520-0450(1977)016<0275:ATTVOC>2.0.CO;2), 1977.

619 Wen, L., Zhao, K., Chen, G., Wang, M., Zhou, B., Huang, H., Hu, D., Lee, W. C., Hu, H.: Drop size distribution
620 characteristics of seven typhoons in China, *J. Geophys. Res. Atmos.*, 123, 6529–6548.
621 <https://doi.org/10.1029/2017JD027950>, 2018.

622 Yang, Q., Dai, Q., Han, D., Chen, Y., and Zhang, S.: Sensitivity analysis of raindrop size distribution parameterizations in
623 WRF rainfall simulation, *Atmos. Res.*, 228, 1–13. <https://doi.org/10.1016/j.atmosres.2019.05.019>, 2019.

624 Yang, Y., Wang, R., Chen, F., Liu, C., Bi, X., and Huang, M.: Synoptic weather patterns modulate the frequency, type and
625 vertical structure of summer precipitation over Eastern China: A perspective from GPM observations, *Atmos. Res.*, 249,
626 105342. <https://doi.org/10.1016/j.atmosres.2020.105342>, 2021.

627 Yao, X., Yang, K., Zhou, X., Wang, Y., Lazhu, C., Chen, Y., and Lu, H.: Surface friction contrast between water body and
628 land enhances precipitation downwind of a large lake in Tibet, *Clim. Dyn.*, 56, 2113–2126.
629 <https://doi.org/10.1007/s00382-020-05575-x>, 2021.

630 Yi, Y., Yi, F., Liu, F., Zhang, Y., Yu, C., and He, Y.: Microphysical process of precipitating hydrometeors from warm-front
631 mid-level stratiform clouds revealed by ground-based lidar observations, *Atmos. Chem. Phys.*, 21, 17649–17664.
632 <https://doi.org/10.5194/acp-21-17649-2021>, 2021.

633